

NSG-2610

**A Critical Assessment of Viscous Models of Trench Topography
and Corner Flow**

Jiajun Zhang

Bradford H. Hager

Arthur Raefsky

June 18, 1984

Seismological Laboratory
California Institute of Technology
Pasadena, California 91125

Abstract

We obtain stresses for Newtonian viscous flow in a simple geometry (e.g. corner flow, bending flow) in order to study the effect of imposed velocity boundary conditions. Stress for a delta function velocity boundary condition decays as $\frac{1}{r^2}$; for a step function velocity, stress goes as $\frac{1}{r}$; for a discontinuity in curvature, the stress singularity is logarithmic. For corner flow, which has a discontinuity of velocity at a certain point, the corresponding stress has a $\frac{1}{r}$ singularity. However, for a more realistic circular-slab model, the stress singularity becomes logarithmic. Thus the stress distribution is very sensitive to the boundary conditions, and in evaluating the applicability of viscous models of trench topography it is essential to use realistic geometries.

Topography and seismicity data from northern Hoshu, Japan, were used to construct a finite element model, with flow assumed tangent to the top of the grid, for both Newtonian and non-Newtonian flow (power law 3 rheology). Normal stresses at the top of the grid are compared to the observed trench topography and gravity anomalies. There is poor agreement. Purely viscous models of subducting slabs with specified velocity boundary conditions do not predict normal stress patterns compatible with observed topography and gravity. Elasticity and plasticity appear to be important for the subduction process.

Introduction

The most remarkable and consistent oceanic bathymetric and geoid features are found near trenches at subduction zones. One of these features is an increase in elevation as the trench is approached from the seaward side. This topographic high, or outer rise, is never more than 500 m above the mean level of the seafloor. Outer rises start between 1000 km and 3000 km seaward of, and crest at about 100 km from, the trench axis. The trench itself is in general a narrow low depression about 100 to 200 km in width, 1.5 to 5 km in depth, and up to 5000 km in length (Grellet & Dubois 1982). The landward side of the trench is marked by a steep increase in elevation which rises to a crest about 2 to 4.5 km above the mean level of the seafloor and consists of either continental crust or an island arc (Ross & Shor 1965, Hayes & Ewing 1970). Gravity observations show variations similar to bathymetry across the trench (Hayes & Ewing 1970, Watts & Talwani 1974, Chapman & Talwani 1982). Other principal observations of the features of subduction zones are their geographic distribution over the world and the seismicity associated with them (e.g., Uyeda & Kanamori 1979, Ruff & Kanamori 1980). These features are similar and coherently distributed over large scales, and they imply a common cause (Le Pichon et al. 1973).

Trench-island arc topography, together with seismic Wadati-Benioff zones, show that the oceanic lithosphere deforms in a continuous manner as it subducts at an oceanic trench. However, understanding the mechanics and dynamics of the subduction process and their relationship to the topography of subduction zones and geometry of the Wadati-Benioff zone has proven to be difficult (Forsyth, 1980).

The rheology of the lithosphere and the physical processes associated with deep-sea trenches are not yet resolved. For example, is the oceanic lithosphere primarily viscous or elastic on the time scale of millions of years? Various theoretical models have been presented to explain the typical shape of plates before their subduction at trenches and the distribution of earthquakes

associated with subduction in terms of bending. Other than the physical features in subduction zones, the surface topography and gravity caused by long term (10^6 years or more) surface loads such as in seamount chains, isolated seamounts, oceanic islands, sediment basins have also been studied using various models. Of these features, the island arc-trench system topography and gravity anomalies are significant for understanding the long term and large scale behavior of the earth because of their universal distribution and similarities and their relation to the mantle convection.

In these models, a mechanically strong lithosphere rests on a much weaker asthenosphere. This mechanically strong lithosphere has been modeled as a uniform elastic plate (Hanks 1971, Caldwell et al. 1976, Parsons and Molnar 1976); a uniform plate with elastic-perfectly plastic rheology, (Turcotte et al. 1978, McAdoo et al. 1978, Chapple and Forsyth 1979); or a uniform viscous plate (DeBremaeker 1977, 1980, McKenzie 1977, Melosh 1978, Melosh & Raefsky 1980). In addition, various rheological models have been suggested by studies of the global gravity field, lithospheric flexure caused by long-term ($>10^6$ years) surface loads, and laboratory experiments (Murrell 1976, Forsyth 1980, Watts et al. 1980, McNutt 1980). All of these models produce trench topography qualitatively similar to that observed. These different rheological models were also proposed to explain other field observations and experimental results (Galand 1979, Liu 1980, Carey & Dubois 1981, Davies 1981). Among these different rheological models, viscous models stem from observations of the rate of postglacial rebound, plate motion, and evidence of thermal convection in the mantle. (Gutenberg 1958, Peltier and Andrews 1976, Isacks et al. 1968, Turcotte and Oxburgh 1967). These long term ($>10^6$ years) and large spatial scale (> 1000 km) phenomena show viscous behavior of the earth's mantle. On the other hand, for short wavelength observations, many authors suggest that surface deformation and the gravity anomalies near trenches are controlled by elastic forces within the deformed plate (Hanks 1971, Le Pichon et al. 1973, Watts and Talwani 1974).

However, numerical experiments for mantle convection (McKenzie 1977) showed that the surface deformation associated with convection in a fluid with a temperature-dependent viscosity bears resemblance to the shape of the ocean floor near trenches. DeBremaeker (1977) showed that a viscous model can be adjusted to fit the general short-wavelength trench profile fairly well. In his model, the shape of a uniform viscous plate is described by a damped sinusoid. Results showed that bending stresses are low, and no regional compressive stress is required. Melosh and Raefsky computed the stresses in a subducting slab using a finite element technique, assuming a viscous constitutive relation (Melosh 1978, Melosh & Raefsky 1980). In this model, the lithosphere was divided conceptually into two parts, a thin elastic lithosphere and a viscous lithosphere. Their principal conclusion is that the first order topographic features of a subduction zone can be explained by viscous stresses generated during subduction in the lower lithosphere beneath a thin elastic upper lithosphere. On the other hand, the thin elastic lithosphere has small effect on these features. Other models based on a viscous half space were used to study flow-induced pressure (Tovish et al. 1978), the angle of subduction (Stevenson and Turner 1977), and the compensation of geoid anomalies due to the subduction of oceanic lithosphere (McAdoo 1982). Sleep (1981) developed a numerical model of fluid dynamics showing that the gravity field observed over the Aleutians near Adak and Amchitka can be explained by a model with power law rheology for the lithosphere near trenches. The underlying assumption in these models is that the oceanic lithosphere near trenches behaves as a viscous fluid over the length scale of a few hundred kilometers (the scale $a < 400$ km used by McAdoo 1982) and the time scale of a few million years.

Seismicity in subduction zones (e.g. Ruff and Kanamori 1980) implies that the strength of coupling between two converging plates (as measured by M_w) is correlated with the age of the subducting oceanic lithosphere and the plate convergence rate. This may imply that the stress in subduction zones is proportional to strain rate, which in turn suggests a viscous rheological behavior.

In order to better understand viscous flow in representative geometries with imposed velocity boundary conditions, we obtain a number of analytical and numerical results for simple test problems. We test the appropriateness of the viscous lithosphere model by investigating some simple test problems as well as more realistic models. The reasons to do this include (1) no study has used actual topographic observations to develop theoretical models and (2) no one has demonstrated that the results obtained from any particular theoretical model are comparable with the realistic case. Later we will show that the stress distribution in viscous flow is very sensitive to velocity and stress boundary conditions. This indicates that it is very important to use observations near subduction zones to construct a viscous flow model for a given individual subducting slab rather than using general theoretical expressions. In order to study the stress distribution in a flow model of realistic geometry of a subducting slab, we use the finite element method, since it has advantages over other methods for models with arbitrary geometry.

We use the topography and seismicity data from the Japan trench to provide constraints on the geometry of finite element models. The Japan trench is one of the best studied trenches. The bathymetric data obtained during 1964 - 1980 (Tomoda and Fujimoto 1982) were used to get an average profile transverse to the Japan Trench near northern Honshu. The linear Wadati-Benioff zone in this region was used to determine the location of the subducting lithosphere. The gravity data in this region clearly resemble the topography data. A detailed analysis of focal mechanism solutions of small and intermediate size earthquakes, together with the seismic coupling (measured by M_w), also contributed to our understanding of the stress state in the slab and the rheological properties of the upper mantle in subduction zones (Kawakatsu & Seno 1983, Ruff and Kanamori 1980, Kanamori 1971, 1977).

We find that the purely viscous models of a subducting slab do not predict a stress pattern compatible with the observed topography and gravity anomalies over the Japan trench. The results from simple test problems indicate that the

discrepancies between observations and numerical results for modeling subducting slabs are general for viscous models. Based on these calculations, we conclude that purely viscous models for the lithosphere do not predict a stress pattern consistent with the actual observations of topography and gravity.

In the following sections, we calculate pressure distributions for the flow induced in a viscous incompressible fluid by the motion of boundaries. First, we discuss half space flow because its simple geometry, then calculate numerical models for more realistic geometries.

Analytic formulations

To understand viscous flow with imposed velocity boundary conditions, we first discuss some analytic results. Later on, we use these results to qualitatively explain the numerical results. The equations of motion for a uniform density, incompressible fluid undergoing steady flow are

$$\eta \nabla^2 \vec{v} = \nabla p \quad (1)$$

$$\nabla \cdot \vec{v} = 0 \quad (2)$$

where η is the viscosity, ρ the density, \vec{v} the fluid velocity, and p the nonhydrostatic or hydrodynamic pressure. In a homogeneous medium, both the density and the viscosity are taken to be constant. If the flow is assumed to be two-dimensional in the x, y plane, it can be described by a stream function, ψ ,

$$\vec{v} = \left(\frac{\partial \psi}{\partial y}, -\frac{\partial \psi}{\partial x}, 0 \right) \quad (3)$$

where $\psi = \psi(x, y)$ satisfies the biharmonic equation

$$\nabla^4 \psi = 0. \quad (4)$$

Any solution of (4) must have the form

$$\psi = \alpha + \beta x + \gamma y \quad (5)$$

where α , β and γ are harmonic (Pearson 1959). For our problems, it is convenient to use the following representation for the stream function:

$$\psi(x,y) = \left\{ A \sinh ky + B \cosh ky + Cy \sinh ky + Dy \cosh ky \right\} \begin{Bmatrix} \sin kx \\ \cos kx \end{Bmatrix} \quad (6)$$

where A,B,C,D are constants to be determined, and k is a wavenumber. Using (3) and (1) both the velocity and the pressure associated with the flow can be determined. Other stress components may then be obtained by :

$$\sigma_{xx} = -p + 2\eta \frac{\partial v_x}{\partial x} \quad (7a)$$

$$\sigma_{xy} = \eta \left(\frac{\partial v_x}{\partial y} + \frac{\partial v_y}{\partial x} \right) \quad (7b)$$

$$\sigma_{yy} = -p + 2\eta \frac{\partial v_y}{\partial y} \quad (7c)$$

The total stress may be obtained by summing the hydrodynamic stress and the hydrostatic stress. The velocity and hydrodynamic stress components corresponding to the flow described by the stream function (6) are given as follows :

$$v_x(x,y) = \left\{ E \sinh ky + F \cosh ky + Dky \sinh ky + Cky \cosh ky \right\} \begin{Bmatrix} \sin kx \\ \cos kx \end{Bmatrix} \quad (8)$$

$$v_y(x,y) = k \left\{ A \sinh ky + B \cosh ky + Cy \sinh ky + Dy \cosh ky \right\} \begin{Bmatrix} -\cos kx \\ \sin kx \end{Bmatrix} \quad (9)$$

$$p(x,y) = p(x,-\infty) + 2\eta k \left\{ C \sinh ky + D \cosh ky \right\} \begin{cases} -\cos kx \\ \sin kx \end{cases} \quad (10)$$

$$\sigma_{xx} = -2\eta k \left\{ G \sinh ky + H \cosh ky + Dky \sinh ky + Cky \cosh ky \right\} \begin{cases} -\cos kx \\ \sin kx \end{cases} - p(x,-\infty) \quad (11)$$

$$\sigma_{xy} = 2\eta k \left\{ F \sinh ky + E \cosh ky + Cky \sinh ky + Dky \cosh ky \right\} \begin{cases} \sin kx \\ \cos kx \end{cases} \quad (12)$$

$$\sigma_{yy} = -2p - \sigma_{xx} \quad (13)$$

where $E = C + Bk$, $F = D + Ak$, $G = 2C + Bk$, $H = 2D + Ak$.

Two dimensional flow in a half space

We consider two-dimensional flow in the half space $y \leq 0$, $-\infty < x < \infty$, for various simple velocity boundary conditions applied at the surface, $y = 0$. We assume velocity goes to zero as y approaches $-\infty$. The various velocity boundary conditions are: i) a harmonic function; ii) a delta function and; iii) a Heaviside unit step function. Using formulae (8) to (13), we obtain some useful results summarized in Table 1, which include stream functions and pressures. Other stress components may also be obtained by these formulae. The fundamental results shown in Table 1 indicate that a point source of horizontal velocity on the surface of a half space generates a region of compression in the forward direction and a region of tension in the backward direction. On the other hand, a point source of upward velocity generates a region of tension beneath this point source and a region of compression elsewhere. A horizontal velocity

discontinuity (step function) produces a region of tension below the discontinuity since it creates a divergence in surface velocity. A discontinuity in the vertical velocity produces an antisymmetric pressure distribution, which is tensional beneath the region with outward velocity.

Although the geometry of the flow is very simple, we found that the results obtained are conceptually useful for understanding the stress distribution of flow with an arbitrary geometry calculated using finite element methods. In order to see how the stress changes due to the variation of the geometry of flow, we study corner flow next for comparison.

Corner flow

The basic corner flow model is discussed by many authors (Batchelor 1970, McKenzie 1969, Stevenson and Turner 1977, Tovish et al. 1978). We assume that the velocities on the surface of the flow are given, and use the same method to calculate the pressure within the corner. The geometry of the flow is shown in Figure 1a. The velocity vectors on the surface have both tangential and normal components. In polar coordinates the stream function is given by

$$\psi(r, \theta) = r (A \sin \theta + B \cos \theta + C \theta \sin \theta + D \theta \cos \theta), \quad (14)$$

where the constants A, B, C, D are to be determined by boundary conditions. Assume that the boundary conditions for the flow within region A (Figure 1a) are

$$\vec{v} = \lambda \vec{a}_r + \alpha \vec{a}_\theta \quad \text{on } \theta = 0 \quad (15a)$$

$$\vec{v} = \mu \vec{a}_r + \beta \vec{a}_\theta \quad \text{on } \theta = \theta_m \quad (15b)$$

where \vec{a}_r is a radial unit vector and \vec{a}_θ the azimuthal unit vector. The velocity may be written as

$$\vec{v} = \frac{1}{r} \frac{\partial \psi}{\partial \theta} \vec{a}_r - \frac{\partial \psi}{\partial r} \vec{a}_\theta \quad (16)$$

The stream function (14) satisfying the boundary conditions has constants A - D

given by

$$A = \frac{1}{\Delta} \left\{ \alpha \theta_m - \beta \theta_m \cos \theta_m + \alpha \sin \theta_m \cos \theta_m - \beta \sin \theta_m - \lambda \theta_m^2 - \mu \theta_m \sin \theta_m \right\} \quad (17a)$$

$$B = -\alpha \quad (17b)$$

$$C = \frac{1}{\Delta} \left\{ \beta \theta_m \sin \theta_m - \alpha \sin^2 \theta_m - \lambda (\sin \theta_m \cos \theta_m - \theta_m) + \mu (\sin \theta_m - \theta_m \cos \theta_m) \right\} \quad (17c)$$

$$D = \frac{1}{\Delta} \left\{ -\alpha \theta_m + \beta \theta_m \cos \theta_m - \alpha \sin \theta_m \cos \theta_m + \beta \sin \theta_m + \lambda \sin^2 \theta_m + \mu \theta_m \sin \theta_m \right\} \quad (17d)$$

$$\Delta = \sin^2 \theta_m - \theta_m^2 \quad (17e)$$

For a Newtonian fluid, the stream function can be written as $\psi = r\theta$, and the pressure is given by

$$p = \frac{-\eta}{r} (\theta'' + \theta') = \frac{2\eta}{r} (C \sin \theta + D \cos \theta) \quad (18)$$

(Tovish et al. 1978). Thus, the pressure corresponding to the boundary conditions (15) is

$$p = \sum_{i=1}^4 p_i \quad (19)$$

$$p_1 = \frac{2\eta}{r} \frac{\lambda}{\Delta} \left\{ \theta_m \sin \theta + \sin \theta_m \sin(\theta_m - \theta) \right\} \quad (19a)$$

$$p_2 = \frac{2\eta}{r} \frac{\mu}{\Delta} \left\{ \sin \theta_m \sin \theta + \theta_m \sin(\theta_m - \theta) \right\} \quad (19b)$$

$$p_3 = \frac{-2\eta}{r} \frac{\alpha}{\Delta} \left\{ \sin\theta_m \cos(\theta_m - \theta) + \theta_m \cos\theta \right\} \quad (19c)$$

$$p_4 = \frac{2\eta}{r} \frac{\beta}{\Delta} \left\{ \sin\theta_m \cos\theta + \theta_m \cos(\theta_m - \theta) \right\} \quad (19d)$$

Since (15) represents any velocity discontinuity for corner flow, the pressure (19) singularity for a velocity discontinuity is of order $1/r$. The results agree with those of Table 1 for $\theta_m = \pi$.

A circular-arc slab model

A more realistic model for subducting slabs is the circular-arc slab model. The surface of the slab is composed of two straight lines on either side of a circular arc of angle θ . This model is shown in Figure 1b, where the subducting slab is a strip of constant thickness in the x, y plane. Using the finite element method, stresses may be obtained for any geometry or boundary conditions. However, for comparison with previous results for half space flow and corner flow, we present an approximate solution for the circular-arc slab model.

Assume the viscosity is constant in the slab, and the velocity along the top surface, which is composed of two straight lines and an arc, is constant and tangential to the surface along its length. Consider the velocity boundary conditions on the top surface of the slab

$$v_x = -v; \quad v_y = 0 \quad \text{at } x \geq 0, \quad y = 0 \quad (\text{horizontal section}) \quad (20a)$$

$$v_x = -v \cos \varphi; \quad v_y = -v \sin \varphi \quad \text{at } \sqrt{x^2 + (y+b)^2} = b, \quad x \leq 0, \quad \varphi \leq \theta \quad (\text{arc section}) \quad (20b)$$

$$v_x = -v \cos \theta; \quad v_y = -v \sin \theta \quad \text{at } x \leq 0, \quad y = 0, \quad \varphi \geq 0 \quad (\text{dipping section}) \quad (20c)$$

where φ is the angle from the beginning of the bend of the slab ($x = 0$) and v is the net convergence rate in the subduction zone. The top surface of the slab in this model has only two changes in curvature. This is a simple model by which we can obtain some insight into the relationship between the stress distribution

and the curvature change. Assume the bottom surface of the slab is traction free.

An exact analytical solution of this problem has not been obtained. A numerical solution for this problem can be obtained by using finite element technique (Melosh & Raefsky 1980). However, by looking at some simple cases, for which we have analytic solutions, it is possible to estimate the stress in a more complex geometry. For the present problem, it is important to estimate stresses near the bending points C: $x = 0, y = 0$, and D: $x = -b \sin\theta, y = b \cos\theta - b$. The following two stream functions describe the flow near these two points. First, the flow in the circular section arc has the stream function

$$\psi = c_1 r^2 \quad (21)$$

and, secondly, the flow in the straight sections has the stream function

$$\psi = c_2 r \sin(\varphi + \alpha) \quad (22)$$

where c_1, c_2 , and α are constants. The two stream functions do not match at points C, D, E, and B, and therefor stress discontinuities appear near these points.

We first show analytically that the singularity in pressure is logarithmic at the bending points C and D. To satisfy the three different boundary conditions (20), the stream functions (21) and (22) become

$$\psi(x,y) = -v(y+b) \quad (23)$$

$$\psi(x,y) = -\frac{v}{2b} [x^2 + (y+b)^2] \quad (24)$$

$$\psi(x,y) = -v [(y+b) \cos\theta - x \sin\theta] \quad (25)$$

respectively. Substituting these three stream functions into (3), we get the velocity at $y=0$

$$v_x = -v; \quad v_y = 0 \quad \text{at } x \geq 0, \quad y=0 \quad (26a)$$

$$v_x = -v; \quad v_y = v \frac{x}{b} \quad \text{at } -b \tan \theta \leq x \leq 0, \quad y=0 \quad (26b)$$

$$v_x = -v \cos \theta; \quad v_y = -v \sin \theta \quad \text{at } x \leq -b \tan \theta, \quad y=0 \quad (26c)$$

If the dip angle of the slab is small or we are only concerned with the region near bending point C, we may assume (26) as the velocity boundary condition for a half space. Using the velocity boundary conditions for the half space, we can make use of the results in Table 1, which we take as Green functions. This is feasible because the problem is linear. Thus, the pressure $p(x,y)$ ($-\infty \leq x \leq \infty, y \leq 0$) can be obtained by superposition:

$$\begin{aligned} p(x,y) = & -\frac{2\eta v}{\pi b} \int_{-b \tan \theta}^0 \frac{[y^2 - (x-x_0)^2] x_0 dx_0}{[y^2 + (x-x_0)^2]} \\ & -v(1-\cos \theta) \left(\frac{\eta}{\pi}\right) \frac{2y}{(x+b \tan \theta)^2 + y^2} \\ & -v(\tan \theta - \sin \theta) \left(\frac{\eta}{\pi}\right) \frac{-2(x+b \tan \theta)}{(x+b \tan \theta)^2 + y^2} \end{aligned} \quad (27)$$

The three terms in (27) are due to the changes of vertical velocity on the segment $-b \tan \theta \leq x \leq 0, y=0$ defined by (26b), the discontinuities of horizontal and vertical velocity at $x = -b \tan \theta, y=0$ respectively. The value of the integral is:

$$I = \frac{1}{2} \ln \frac{y^2 + (x+b \tan \theta)^2}{x^2 + y^2} - \frac{b \tan \theta (x+b \tan \theta)}{(x+b \tan \theta)^2 + y^2} \quad (28)$$

The pressure is

$$p = \frac{2\eta v}{\pi} \frac{(x+b \tan \theta) (2 \tan \theta - \sin \theta) - y (1 - \cos \theta)}{(x+b \tan \theta)^2 + y^2}$$

$$-\frac{\eta v}{\pi b} \ln \frac{y^2 + (x + b \tan \theta)^2}{x^2 + y^2} \quad (29)$$

There are other ways to estimate stresses in the slab but the above approximation is simple and adequate for estimating the stress in the region near the singular point $x = 0, y = 0$. The approximation does not predict the velocities defined by (20) on the section of $\varphi \geq \frac{\theta}{2}$ as accurately as those where $\varphi \leq \frac{\theta}{2}$. Hence this expression is only an approximate solution for the pressure in the region near the singular point $x = 0, y = 0$, and is ineffective for the region $\varphi \geq \frac{\theta}{2}$. The equation (29) shows that the pressure is logarithmically singular at the point $x = 0, y = 0$. Since the problem for circular arc is antisymmetric about $\varphi = \frac{\theta}{2}$, the pressure associated with the condition (29) has two logarithmic singularities at point C and D on the top surface of the slab. Formula (29) shows that the logarithmic singularity is tensional at point C, and compressional at point D by the antisymmetry of the problem.

Using finite element methods, pressure profiles along lines near the top surface for this slab model have been calculated for comparison with the approximate solution (29). Figure 2 shows the pressure profiles along two lines parallel to the top surface of the slab calculated using formula (29), P_a , and the finite element method, P_f . In figure 2, the distance d between each line and the top surface is given in units of the thickness H_v of the slab, as is the horizontal distance measured from the beginning of the bend, point C. Pressure has units of $\eta v / H_v$. Near point C, the pressure profiles from the finite element calculation P_f and approximate solution P_a agree well. Although the value of the pressure at point C for the approximate analytic solution, P_a , is infinite, the values outside a small neighborhood of point C agree well with P_f . Since we have ignored the influence of the lower boundary of the slab, (29) is only valid near the surface of the slab. This is why we did not get a singular point at point B.

From the stresses obtained in Table 1, those for corner flow and those for bending flow, we see that the stress distribution is very sensitive to imposed velocity boundary conditions. Stress for an impulsive velocity boundary condition behaves as $\frac{1}{r^2}$; for a step function velocity, stress goes as $\frac{1}{r}$; and for a discontinuity in curvature, the stress singularity is logarithmic. For corner flow, which has a discontinuity of the vector velocity at certain point, the corresponding stress has a $\frac{1}{r}$ singularity at that point. However, for the more realistic circular-slab model, the stress singularity becomes logarithmic. The geometry of seismic Wadati-Benioff zones around the world shows that the curvature of subducting slabs probably varies from the outer rise down to the upper mantle (Isacks & Barazangi 1977). Since the stress pattern is sensitive to the change in curvature, the corner flow model is probably not a good model to study detailed stress distributions in subduction zones.

Finite element calculations for Melosh & Raefsky's models

The problem of subduction of a viscous slab may be solved numerically, as was done previously by Melosh & Raefsky, 1980. Melosh (1978, Melosh & Raefsky, 1980) assumed that the lithosphere could be treated as two parts : an elastic upper part, 15 to 25 km thick (H_e), and a viscous lower part 50 - 80 km thick (H_v). The asthenosphere is a zone of low viscosity lying below this lithosphere. Melosh and Raefsky assumed that the elastic bending stresses are unimportant, and elastic stresses are not included in their calculations.

Their calculations show the following results. As the lithosphere subducts and bends downward, extensional flow in the upper part of the very viscous layer produces a zone of extensional normal stress. If, as they suppose, the stress propagates through the elastic layer to the surface without significant changes, this extensional stress will produce a topographic low, where the oceanic trench is located. The topographic high on the landward side of the trench is due to a zone of compressive stresses. As their model produced qualitatively reasonable

results, we wished to investigate it further using more realistic geometries. We first attempted to reproduce their results.

Melosh and Raefsky (1980) used two finite element grids. One has continuous curvature along its top surface with error function derivatives, while another is the circular-arc grid, with the geometry of the circular-arc slab model we have used above. Since the numerical results for these models are important for modeling the subduction zone, we discuss these models in detail. We studied these models by using finer grids than that shown in Figure 2 of their paper, and analyzed the results for different boundary conditions. Following Melosh and Raefsky, we do not include the elastic layer in our present calculations. While they used a Maxwell viscoelastic rheology and calculated its steady-state response, we posed the problem as incompressible creeping flow and solved the problem using a penalty function formulation (Hughes & Taylor 1978).

The boundary conditions for the viscous part of the lithosphere are as follows. The base of the lithosphere is free of stress other than hydrostatic pressure, and the velocities on the top of the viscous lithosphere are specified.

To have adequate resolution of stresses for the circular-arc slab model, we used a fine grid. The numbers on the Figure 3a give the numbers of elements along each part of the grid. A total of $15 \times (16+8+45+19+10) = 1470$ bilinear isoparametric elements were used. The velocity boundary conditions (20) are applied to the grid such that the velocity vectors are tangent to the upper line of the grid. The left end of the slab is subject to constant velocity. The right side of the slab has the same velocity boundary condition as that of the horizontal section. These are given as:

$$v_x = -v, \quad v_y = 0 \quad \text{at the right side of the grid (30a)}$$

$$v_x = -v \cos \theta, \quad v_y = -v \sin \theta \quad \text{at the left side of the grid (30b)}$$

The results for the calculated pressures are shown in Figure 3. Figure 3a shows the pressure contours for the model. The contours are symmetric and

have four singularities at points B, C, D, and E (Figure 1b). The two singularities on the top are logarithmic. Figure 3b is a plot of the pressure along the top line of nodes of the grid.

The derivative of the prescribed velocity (20) is discontinuous at the beginning and end of the bend. To alleviate this discontinuity, Melosh & Raefsky (1980) suggested employing a smoothed velocity profile in the circular arc section given by

$$v_y = \begin{cases} \frac{-v \sin \varphi}{2} [1 - \cos(\frac{2\pi \varphi}{\theta})] & ; 0 < \varphi < \frac{\theta}{2} \\ \frac{-v \sin \varphi}{2} [1 - \cos(\frac{2\pi \varphi}{\theta})] - \frac{v \sin \theta}{2} [1 - \cos(\frac{2\pi \varphi}{\theta})] & ; \frac{\theta}{2} < \varphi < \theta \end{cases} \quad (31a)$$

$$v_x = -\sqrt{v^2 - v_y^2} \quad (31b)$$

Using the velocity boundary condition above, the stress curves calculated along a line parallel to the top surface of the slab have a small uplifted region or bench. Since the bench was not fully resolved in Melosh & Raefsky's paper (1980), we calculated the stress using a finer grid. The grid used has 1400 elements, and the size of the elements near the edges of the grid is much smaller than that of the elements near the center line. Figure 4a shows the pressure contours for the circular-arc grid with smoothed velocity boundary conditions (31). Note the differences between the pressure contours in Figure 3a and 4a. In Figure 4a, the maximum and minimum values of pressure move toward the bend axis and spread out, losing their sharp points. Figure 4b is the pressure profile along the top layer of the finer grid. This pressure profile is smooth and does not have sharp points at the two ends of the bend. By inspecting similar plots for nodes at depth in the slab, we find that the amplitude of the bench near the bend axis is most pronounced at the surface and decreases with depth.

In the stress analysis for the corner flow and the circular-arc slab model, as shown in previous sections, discontinuities of velocity or its derivatives produce local stress variations. The circular-arc slab model has discontinuous

derivatives of vertical velocity, and thus its curvature. The stresses for the model have logarithmic singularities. In this case, we have different velocity profiles applied to the surface of the grid on each side of the bend axis, where they have discontinuities of the second derivatives of velocity. These discontinuities also produce local variations of stress, which causes the bench in the stress profiles.

Comparing the pressure distributions for the circular-arc slab grid with the two slight different velocity boundary conditions we used above, we see that for a particular grid, the stress is very sensitive to velocity boundary conditions. In order to study the effect of different grid geometries, we also investigated a finite element model with an error function velocity profile, given as

$$v_y = -\frac{v \sin \theta}{2} \operatorname{erfc} \left(\frac{S}{S_c} \right) \quad (32)$$

$$v_x = -\sqrt{v^2 - v_y^2}$$

where S is the arc distance from the bend and the cut-off parameter S_c is given by

$$S_c = \frac{2R}{\sqrt{\pi}} \sin \left(\frac{\theta}{2} \right) \quad (33)$$

Using the same boundary conditions on two different grids, we find that stress distribution patterns are quite similar. One grid is the circular-arc grid used previously (Figure 3a), and the other is a rectangular grid, i.e. a flat slab with no dipping region. Figure 5(a-1), 5(a-2), and 5(a-3) show 3 different velocity profiles which correspond to 3 different 'cut off' parameters of the error function velocity (32) and (33). Applying these velocity profiles to the circular-arc grid in Figure 3, we have pressure profiles at the surface, Figure 5(b-1), 5(b-2), and 5(b-3). For a rectangular grid, we have pressure profiles 5(c-1), 5(c-2), and

5(c-3). Comparing these pressure curves and velocity profiles, we notice that for the same velocity boundary conditions, the difference in the magnitude of the maximum tension is about 20 percent for the 2 different grids. However, the shape of the pressure curves is quite similar. Since, for the same grid, the stress patterns are very different for different velocity conditions, the stress variation is more strongly controlled by velocity boundary conditions than by the geometry.

According to equation (9), the velocity gradient $\nabla \vec{v}$ causes stresses in viscous flow. From the results in Table 1, we can understand in a general way the results obtained by the finite element method. We consider the velocity vector along a particular stream line. At each point along the stream line we have two characteristic directions, tangent and normal to the stream line, respectively. We project the velocity vectors of a small segment of the stream line onto these two directions, and call the variations of the two components along the streamline tangential and normal gradients. The gradients defined above are discrete; for example, the tangential and normal gradients are zero on the right side of the slab of point C in Figure 1b. The normal gradients are negative, the tangential gradient is zero on the entire circular arc for constant tangential velocity boundary conditions. At point C and D, we have nonzero normal and tangential gradients. From the fundamental solutions for the half space flow in Table 1, we see that tangential gradients cause tension, while normal gradients cause compression followed by tension. Since the fundamental results referred to in Table 1 are for a half space, this kind of intuition is effective only for flow like our thick plate model.

The stress distribution obtained from the finite element calculations, in particular, the stress variation near the bending point, can be explained using the analytical results. In Figure 3, the pressure is compressional to the right of the bending point C. Near C, the pressure changes sign becoming tensional and then increases rapidly to a tension maximum at C.

Before the bend, the normal and tangential gradients are both zero. After the bend begins, the normal gradient of velocity becomes nonzero, being negative to the left of point C. But the tangential gradient is negative near C and zero to the left of it (Figure 6). This is the reason that the maximum tension appears at the bending point C. The compression before the point C is caused by the negative tangential gradients near point C. The pressure distribution near the end point, D, of the arc can also be explained by negative normal and positive tangential gradients.

Figure 7 shows the superposition of pressure due to the normal velocity gradients for a series of vertical step function velocity discontinuities. The reason that the pressure near the bend axis tends to be zero in the unsmoothed boundary condition calculations is that, although the normal gradient there is negative (Figure 7), the total pressure will vanish near the bend axis by superposition of the stresses due to a series of vertical step function velocity discontinuities.

The above discussion can be extended to explain the 'bench' phenomenon found in Melosh & Raefsky's (1980) finite element calculations. From the analysis of the circular-arc model, we know that by applying a tangential velocity boundary condition, the model produces reasonable results, which match the approximate analytic solution. In Figure 3, the bench does not occur. However, Figure 4 shows a bench near the bend axis. The only difference between these two models is that slightly different velocity boundary conditions are used. Subtracting the two velocity profiles, we obtain a differential velocity boundary condition. Applying this boundary condition to the same grid, we obtain the results shown in Figure 8(b-2).

Figure 8a shows three velocity boundary conditions for the circular-arc model of Figure 3a. Since the smoothed velocity boundary condition differs from the unsmoothed velocity boundary condition only on the circular arc parts of the grid, only the velocities of smoothed, unsmoothed, and their difference

are plotted. They are unsmoothed vertical velocities A_y and horizontal velocities A_x , smoothed vertical velocities B_y and horizontal velocities B_x , and their differences C_y , C_x . The differential velocities C are also plotted on coordinates with the origin at the bend axis and a 45° rotation of the original coordinates (Figure 8(a - 2)). Note that 8(a - 1) shows that the unsmoothed vertical velocities A_y and differential velocities C_y have derivative discontinuities at the beginning and the end of the bend which have the same magnitudes but reverse signs. Figure 8(b - 1), 8(b - 2), and 8(b - 3) show the pressure profiles along the top line of the grid. They correspond to unsmoothed, differential and smoothed velocity boundary conditions respectively. Both unsmoothed and differential velocity boundary conditions produce logarithmic singularities at the beginning and end points of the bend. They have opposite signs and are canceled in the calculations with smoothed velocity boundary conditions. The bench occurs in the calculations with the differential velocity boundary condition, since it arises in calculations with the smoothed boundary condition.

In order to explain the occurrence of these three pressure profiles intuitively, Figure 8 shows a rough scheme explaining how the smoothed pressure is obtained. 8(c - 1) shows the normal gradient g_{\perp} of velocity on the arc, which is a (negative) constant for the unsmoothed velocity. 8(c - 2) is the pressure profile along the top line of the grid produced by the velocity. 8(d - 1) shows the residual or differential normal velocity gradients g'_{\perp} corresponding to the differential velocity. 8(d - 2) shows the two logarithmic singularities and a bench produced by the residual normal gradients. 8(a - 1) and 8(a - 2) also show that the tangential velocity gradient is very small compared to the normal gradient for the differential velocities, and does not make as significant a contribution to the stress on the arc section as the normal gradients do (Figure 8c and 8d). The important finding is that the 'bench' is not the result of sharp bending and unbending of the slab, but rather is the result of a small kink in velocities, resulting from smoothing the velocity boundary condition near the axis of the bending slab. The choice of the smoothing function produces a

'bench' which severely distorts the stress distribution near the bending axis at shallow depth. One must therefore be extremely careful in interpreting the results of numerical models in a subduction zone type geometry; small differences in velocity boundary conditions affect the stress qualitatively as well as quantitatively.

Models using observed grids for the Japan trench

From the above discussion, we can see that for the flow models addressed, the stress distribution is very sensitive to velocity boundary conditions. Thus, instead of using a simple theoretical model, it is necessary to construct viscous flow models with more realistic geometries for individual subducting slabs.

The path of the subducted plate in the upper mantle is usually delineated by a zone of earthquakes which occur in the upper part of the plate, but the detailed relationship between the upper surface of the descending plate and the seismic zone may not always be clear. However, for the Wadati-Benioff zone near the Northern Honshu Arc, Japan, detailed seismicity studies show that earthquakes with the same mechanism are systematically distributed (Kawakatsu et al. 1983).

We assume that the planar structure of seismicity represents the geometry of the subducting plate. This is probably true for thrust type earthquakes which have a seismic slip front identical to the aseismic front defined as the seaward edge of the aseismic mantle wedge beneath the island arc (Yoshii 1975). Thus the approximate location and dip of the interface between the two converging plates are indicated by the shallow thrust zone and deep thrust zone (Kawakatsu and Seno 1983). We assume that there is no sharp bending of the oceanic plate in the asthenosphere, and consider the upper envelope of the epicenters of mantle earthquakes as the upper surface of the subducting plate. These constraints are similar to those of Isacks and Barazangi (1976). The thrust and compressional type earthquakes in cross sections of the whole Northern Honshu Arc were

digitized. A polynomial curve was generated by a least squares fit to these epicenters to obtain the geometry of the interface between the two converging plates. Another polynomial, which fits the averaged topography data, has a small offset 50 km landward from the trench from the polynomial which fits the Wadati-Benioff zone (1.154 km below the topography polynomial). In obtaining the least squares polynomial, we did not consider the data points near the seamount (Tomoda and Fujimoto 1982). The profiles of topography corresponding to the boundaries between the four seismic sections of Kawakatsu and Seno (1983) were obtained by digitizing the bottom topography map in this region (Tomoda and Fujimoto 1982). We construct a finite element grid assuming that the thickness of the viscous lithosphere (H_v) is constant and equal to 50 km.

The boundary conditions for the models are as follows: The base of the lithosphere is free of shear stress and normal stress other than that due to hydrostatic pressure. At the top surface of the viscous lithosphere, the velocity is constant and tangent to the surface of the lithospheric slab. For the down going side of the viscous lithosphere, at the depth of the deepest earthquake in the data (about 180 km deep), the velocity is parallel to and equal to the velocity on the surface of the lithosphere. On the oceanward edge of the viscous lithosphere, the velocity is also defined as a constant and parallel to the upper surface.

We assume that the steady state bending of the elastic plate forces the upper surface of the viscous layer to move with a constant tangential velocity, also assuming that the thickness of the upper elastic layer does not change. We note that the double seismic zones are almost parallel over 200 km from the trench. This may imply that there is no significant change of the thickness of the subducting slab. Although the velocity along the upper surface may change from place to place because of coupling and uncoupling of the two converging plates, as a first approximation, we assume it is constant and tangent to the surface, as the basic question here is, to first order, whether or not the topography of the island trench-outer rise system can be supported by the viscous stresses

in the flow of a viscous layer beneath an elastic lithosphere. The free stress condition at the base of the viscous layer is appropriate if one considers the asthenosphere as a zone of low viscosity underlying the lithosphere.

Since the position of the interface between the two converging plates is uncertain, several grids which have slightly different geometries of their upper boundaries were used. These boundaries are determined by polynomials which fit the upper envelope of the hypocenters somewhat differently. These grids differ slightly from each other with respect to bending curvature and depth of the interface of the two converging plates. Finite element calculations show that although these models yield somewhat different results, none adequately predict the trench topography. As the implications from different models are quite consistent, we will discuss those features of the models which do not depend on the geometry of the grids. Figure 9 shows two of the models used in our finite element calculations with slightly different geometry. The models shown in Figure 9a and 9b, will be called model A and B respectively.

The upper boundary of the grid of model A is an estimate of the top surface of the descending lithosphere based upon the following constraints. The bottom topography of the sea is taken to be the upper surface of the plate just before thrusting beneath the landward plate. Figure 10 shows a bathymetric profile east of Northern Honshu as a function of distance from trench. It ranges from the trench ($x = 0.0$) to 900 km ($x = 18.0$) seaward. It was obtained by averaging 5 cross sections of topographic profiles from 450 km west to 900 km east of the trench axis. These cross sections correspond to the boundaries of 4 seismicity cross sections used by Kawakatsu and Seno (1983). The top lines of the two finite element grids, for model A and model B are also plotted in Figure 10. The two curves (upper surface of the grid) fit the topography very well in general. At 500 km from the trench there is a 50 km wide 300 m high upper swing. It results from averaging the topography data including a seamount in the fifth section. Except for this, the sea floor is quite flat at that distance. Figure 10 also shows the outer rise is 500 m above the sea floor and 500 km wide. Model B differs

from model A slightly in curvature.

Observed grid with constant Newtonian viscosity

We present the stresses calculated for model A, assuming a constant Newtonian viscosity. Figure 11 shows the stress components T_{xx} , T_{yy} , and pressure P as functions of distance from the trench for the top surface of the model. To calculate the predicted topography from the viscous stresses, we assume a simplified situation in which the normal stresses T_{yy} at the top surface of the viscous lithosphere are fully compensated by a decrease in elevation of the overlying rock:

$$W = -T_{yy}/(\rho_m - \rho_w)g \quad (34)$$

where W is the decrease in the depth of the sea floor, T_{yy} is the normal stress at the base of the elastic lithosphere, ρ_m is the mantle density, ρ_w is the density of the seawater and g is the acceleration of gravity. In this case, the normal stress T_{yy} produced by flow in viscous lithosphere is proportional to the depth of the sea floor. For the vertical stresses T_{yy} from 800 km seaward to 250 km landward of the trench axis obtained in our model, there is a maximum tension of 7×10^6 Pa, 200 km landward of the trench and a maximum compression of 5×10^5 Pa, 140 km seaward of the trench. Denoting the x_t and x_r as the distances from predicted trench axis and outrise to the actual trench axis, W_t and W_r as the corresponding topography from sea floor (positive up) and assuming $\rho_m = 3300 \text{ kg m}^{-3}$, $\rho_w = 1000 \text{ kg m}^{-3}$, $g = 10 \text{ ms}^{-2}$, we obtained the predicted topography $x_t = -200 \text{ km}$, $W_t = -300 \text{ m}$, $x_r = 140 \text{ km}$, and $W_r = 20 \text{ m}$. This does not agree with the actual topography even qualitatively.

The above assumption neglects the ability of the elastic part of the lithosphere (the upper 15 - 30 km) to transmit normal forces to moderate distance. For an elastic lithosphere loaded by vertical stresses T_{yy} applied at its base, the deflection W can be calculated by:

$$W(x) = -\frac{\alpha^3}{8D} \int_{-\infty}^{\infty} e^{-\frac{|x-s|}{\alpha}} \left(\cos \frac{x-s}{\alpha} + \sin \frac{|x-s|}{\alpha} \right) T_{yy}(s) ds \quad (35)$$

where

$$D = \frac{E H_e^3}{12(1-\nu^2)} \quad (35a)$$

$$\alpha = \left[\frac{4 D}{(\rho_m - \rho_w)g} \right]^{1/4} \quad (35b)$$

E is the Young's modulus, H_e is the thickness of the elastic lithosphere, ν is Poisson's ratio, D is the flexural rigidity and α is the flexural parameter (Turcotte and Schubert 1982). The elastic part of the lithosphere can be considered as a filter with flexural parameter usually assumed to be 40 to 75 km (Walcott 1970, Watts et al. 1975, McNutt & Menard 1978). Deflections due to normal forces with wavelengths much longer than the flexural parameter are transmitted through the elastic lithosphere essentially unaltered.

Using the viscous stresses obtained in our model, we calculated the deflection of the elastic lithosphere by formula (35). The viscous stress T_{yy} obtained from our model has wavelength about 500 km (Figure 11), so it can be transmitted through the flexible elastic lithosphere resulting in the surface topography proportional to the stresses. The vertical stresses T_{yy} used in the calculation include the stresses from 800 km seaward to 250 km landward of the trench. Assuming $\nu = 0.25$, we obtained the predicted topography shown in Table 2. Table 2 shows that for $E = 70$ GPa, which is a reasonable value for an oceanic lithosphere, the flexural parameter α is much smaller than the wavelength of the load applied at the base of the elastic lithosphere by viscous stresses, and the deflections due to the normal force are transmitted through the the elastic lithosphere essentially unaltered. The predicted topography of the elastic lithosphere due to the vertical stress T_{yy} does not agree with actual topography.

If the upper surface of the elastic lithosphere is traction free, a stress σ_{xx}^{el} due to the shear stress σ_{xy}^b applied at the base of the elastic lithosphere by the viscous flow, must appear in the elastic lithosphere:

$$\sigma_{xx}^{el} = \frac{1}{H_e} \int_{-x}^x \sigma_{xy}^b(x') dx' \quad (36)$$

where σ_{xy}^b is the shear stress on the base of the elastic lithosphere (Melosh and Raefsky 1980, equation (3)). From the viscous stresses obtained for model A, the calculated elastic stress (36) has a sign which is inconsistent with normal faulting in the outer trench region.

Shown in Figure 12a, 12b, and 12c are contour plots for T_{xx} , T_{yy} and pressure, respectively. Figure 12d shows the orientation and magnitude of the principal compressional stresses in the slab at the center of each element. The stress pattern is very different from that of the circular arc slab model. From the top surface to the bottom surface of the lithosphere, compressional stress T_{xx} increases in magnitude on the seaward side, while the pressure P and the vertical stress T_{yy} decrease. On the landward side, pressure is compressional on the top surface and tensional on the bottom surface.

Another model with a different shape of the top surface but the same boundary conditions (model B) was tested. In model B, the top surface has a small dip angle. The difference between the two models is very small. Models with buoyancy force due to average density differences between the subducting slab and asthenosphere with a Newtonian viscosity were also considered. We assume there is a 0.0665 g/cm^2 average density contrast between the cooling slab and the mantle (Hager & O'Connell 1981). The results near the trench are similar with those described above, and become more tensional at depth.

Observed grid with non-Newtonian Viscosity

We also investigate the effects of the possible nonlinear dependence of viscosity on stresses. A constitutive law for non-Newtonian viscosity often used in the literature is:

$$\dot{\epsilon}_{ij}|_{\text{steady state}} = \left(\frac{1}{2\eta_{\text{eff}}}\right)\sigma_{ij} \quad (37)$$

where $\dot{\epsilon}_{ij}$ is the strain rate, η_{eff} is effective viscosity, which is stress dependent, and σ_{ij} is the stress tensor. The effective viscosity for a power law fluid is

$$\eta_{\text{eff}} = \eta_n / \sigma^{n-1} \quad (38)$$

where σ is the square root of the second deviatoric stress invariant and η_n is a constant (when $n = 1$, it is identical to the viscosity). Figure 13 shows the stresses for model A for a power law rheology with $n = 3$. The constant η_n does not depend upon depth. The general features of these plots are much different than those found for a Newtonian viscosity. In the region with small stresses seaward of the trench, the stress pattern becomes complicated, more asymmetric, and more sensitive to the velocity boundary conditions. The pressure near the trench becomes compressional and the region of tensional vertical stress T_{yy} moves farther away from the trench. This model does not predict the actual topography.

By changing boundary conditions, we were able to find a model which predicts a vertical stress pattern similar to the trench topography. In this model, the slab begins bending on the seaward side of the trench, inconsistent with the actual topography. Since a very small change of the geometry of the model leads to significant variation of the stresses obtained, it is most unlikely that such a model is reasonable for the unique feature of trench topography of the world.

Concluding Remarks

The most important result of this work is that the analytic and numerical calculations for the stresses in a bending viscous flow show that the stress pattern is very sensitive to the velocity boundary conditions. The vertical stresses T_{yy} for non-Newtonian flow are more complex and asymmetric than for the Newtonian flow model. Regions where stresses are small are relatively more perturbed than regions where stresses are large, and the transition from vertical tension to compression does not move in the direction to predict actual topography.

For a non-Newtonian fluid with a power law 3 rheology, small stresses correspond to a higher viscosity, and are more sensitive to strain rate changes than for the Newtonian fluid. In our model, for the non-Newtonian flow, stresses near the trench are lower than for the deep part of the slab, and more complex than in Newtonian flow. This shows that in the region near the trench, the strain rate changes in the subducting slab, which are probably larger than in the other part of the slab, do not induce large stress variations as is expected in viscous flow. This suggests that topography near trenches is a solid deformation phenomenon rather than viscous flow Phenomenon.

The primary purpose of this paper is to see if the first order topography and gravity field of subduction zones can be explained by viscous stresses generated in the lower viscous lithosphere during its subduction. Finite element models have been developed previously to explain the topographic structure of subduction zones (Melosh & Raefsky 1980). However, the two models did not use realistic geometries. In their first model, the geometry of the upper surface of the viscous lithosphere is prescribed by error function profiles, which are not representative of actual subducting slabs. Although the stress T_{yy} obtained for the model is similar to observed topography, the sensitivity of stress distribution to velocity boundary conditions, which are determined by the geometry of the slab, makes the result for any model with particular geometry not

applicable to other models, even approximately. Second, the results for the model with a circular arc velocity profile are complicated by the smoothing procedure, as explained in Part 1 of this paper.

Summarizing the finite element computations for observed grids, we find:

1) The stresses near the top surface are very sensitive to the velocity boundary conditions. 2) The viscous stresses do not have a pattern which is related even qualitatively to the topography near trenches, if the observed geometry is used to derive velocities.

Similar problems caused by the sensitivity of stresses to the velocity boundary conditions exist in modeling the flow in the mantle outside the cold slab. Several authors used the corner flow model to investigate the torque balance on the slab (Stevenson and Turner 1977), mantle flow pressure and viscous coupling between the overriding plate and the down going slab (Tovish et al. 1978), and the compensation of geoid anomalies due to subducting slabs (McAdoo, 1982). When McKenzie (1969) first proposed to use corner flow to study the flow within the mantle, he emphasized that there was some doubt whether the resulting solutions apply to the flow in the earth, and in this respect there was a considerable contrast between the section of the flow in the mantle and the previous sections of his paper. In the corner flow model, there is a velocity jump at the trench which makes the solution singular at the trench axis. This singularity determines the whole solution pattern, and makes the solution inapplicable quantitatively to actual subduction zones in the distance range of the length of the slab, although it is valid qualitatively.

The results of our models using observed geometries as constraints show diverse stress patterns, out of phase with the actual topography and gravity. The conclusion is that the topography and geoid anomalies associated with trenches are supported by the strength of the strong upper lithosphere which behaves as an elastic-plastic solid at the appropriate time scale.

Topography appears to be an effective discriminant in determining the appropriate rheological model for the lithosphere. Study of the topography of an actual subduction zone suggests an elastic-plastic rheology for oceanic lithosphere. More precise results may be obtained by applying the finite element method to an elastic-plastic layer overlaying a viscous layer. It appears that sophisticated methods and accurate data are necessary for a better understanding of the lithosphere's behavior.

Although the sensitivity of stress to the velocity boundary condition diminishes the possibility that viscous stress supports the topography, the viscous behavior of subducting slab is obvious in many aspects as discussed in the introduction. Viscous stresses acting on the elastic lithosphere may play a more important role in the dipping section than in the bending and horizontal section of the elastic lithosphere.

Consider the lithosphere model described in Figure 1a of Melosh 1978. In our calculations, we find that the stress pattern in the viscous slab after bending is stable. In Figure 12, the deviatoric stresses show that the tensional axis is parallel to the slab. This result is in accord with the existence of tensional events in the lower part of the upper lithosphere. Small changes of velocities caused by the interaction of two converging plates may enhance or diminish the tensional stress. Enhanced tensional stresses in the lower surface of the upper lithosphere will make upper compressional events become tensional or make the double seismic zone a tensional zone. Diminished tensional stresses in the lower surface of the upper lithosphere are favorable a single one compressional zone.

Acknowledgements

We thank Keith Echelmeyer, Luciana Astiz, Ronan LeBras, Patricia F. Scott, and Robert Svendsen for helpful comments on the manuscript. This work was supported by NASA grant NSG-7610 and an Alfred P. Sloan Foundation Fellowship

(BHH). Contribution No. 4120, Division of Geological and Planetary Sciences, California Institute of Technology, Pasadena, CA 91125, USA.

References

- Batchelor, G. K., 1970. Introduction to Fluid Dynamics, Cambridge University Press, Cambridge.
- Caldwell, J. G. & Haxby, W. F. & Turcotte, D. L., 1976. On the applicability of a universal elastic trench profile, *Earth Planet. Sci. Lett.*, 31, 239-246, 1976.
- Carey, E. & Dubois, J., 1981. Behaviour of the oceanic lithosphere at subduction zones; plastic yield strength from a finite-element method, *Tectonophysics*, 74, 99-110.
- Chapman, M. E. & Talwani, M., 1982. Geoid anomalies over deep sea trenches, *Geophys. J. R. astr. Soc.*, 68, 349-369.
- Chapple, W. M. & Forsyth, D. W., 1979. Earthquakes and bending of plates at trenches, *J. geophys. Res.*, 84, 6729-6749.
- Davies, G. F., 1981. Regional compensation of subducted lithosphere: Effects on geoid, gravity, and topography from a preliminary model, *Earth Planet. Sci. Lett.*, 54, 431-441.
- DeBremaecker, J. C., 1977. Is the oceanic lithosphere elastic or viscous ?, *J. geophys. Res.*, 82, 2001-2004.
- DeBremaecker, J. C., 1980. Correction, *J. geophys. Res.*, 85, 3952.
- Forsyth, D. W., 1980. Comparison of mechanical models of the oceanic lithosphere, *J. geophys. Res.*, 85, 6364-6368.
- Galand, D. G., 1979. Introduction to Geophysics (mantle, core and crust), 2nd Ed., W. B. Saunders Company, Philadelphia.
- Grellet, C. & Dubois, J., 1982. The depth of trench as a function of the subduction rate and age of the lithosphere, *Tectonophysics*, 82, 45-56.
- Gutenberg, B., 1958. Rheological Problems of the Earth's Interior, in Eirich (1958). Vol. 2., p. 401.
- Hager, B. H. & O'Connell, R. J., 1981. A simple global model of plate dynamics and mantle convection, *J. geophys. Res.*, 86, 4843-4867.
- Hanks, T. C., 1971. The Kuril trench-Hokkaido rise system: large shallow

- earthquakes and simple models of deformation, *Geophys. J. R. astr. Soc.*, 23, 123-189.
- Hayes, D. E. & Ewing, M., 1970. Pacific boundary structure, in *The Sea*, Vol. 4, Part II, pp. 27-72, ed. Maxwell, A. E., Wiley & Sons, New York.
- Hughes, T. J. R. & Taylor, R. L., 1978. Unconditionally stable algorithms for quasi-static elasto/viscoplastic finite element analysis, *Comput. Struct.*, 8, 169-173.
- Isacks, B. L., Oliver, J. & Sykes, L. R., 1968. Seismology and the new global tectonics, *J. geophys. Res.*, 73, 5855-5899.
- Isacks, B. L. & Barazangi, M., 1977. Geometry of Benioff zones: lateral segmentation and downwards bending of the subducted lithosphere, in *Island Arcs Deep Sea Trenches and Back-Arc Basins*, edited by M. Talwani and W. C. Pitman III, American Geophysical Union, Washington, D.C.
- Kanamori, H., 1971. Great earthquakes at island arcs and the lithosphere, *Tectonophysics*, 12, 187-198.
- Kanamori, H., 1977. Seismic and aseismic slip along subduction zones and their tectonic implications, in *Island Arcs Deep Sea Trenches and Back-Arc Basins*, edited by M. Talwani and W. C. Pitman III, American Geophysical Union, Washington, D.C.
- Kawakatsu, H. & Seno, T., 1983. Triple seismic zone and the regional variation of seismicity along the Northern Honshu arc, *J. geophys. Res.*, 88, 4215-4230.
- Le Pichon, X., Francheteau, J. & Bonnin, J., 1973, *Plate Tectonics*, Elsevier, Amsterdam.
- Liu, H. P., 1980. The structure of the Kurile Trench-Hokkaido Rise system computed by an elastic time-dependent plastic plate model incorporating rock deformation data, *J. geophys. Res.*, 85, 901-912.
- McAdoo, D. C., Caldwell, J. G. & Turcotte, D. L., 1978. On the elastic-perfectly plastic bending of the lithosphere under generalized loading with application to the Kurile trench, *Geophys. J. R. astr. Soc.*, 54, 11-26.

- McAdoo, D. C., 1982. On the compensation of geoid anomalies due to subducting slabs, *J. geophys. Res.*, 87, 8684-8692.
- McKenzie, D. P., 1969. Speculations on the consequences and causes of plate motions, *Geophys. J. R. astr. Soc.*, 18, 1-32.
- McKenzie, D. P., 1977. Surface deformation, gravity anomalies and convection, *Geophys. J. R. astr. Soc.*, 48, 211-238.
- McNutt, M. K. & Menard, H. W., 1978. Lithospheric flexure and uplifted atolls, *J. geophys. Res.*, 83, 1206-1212.
- McNutt, M., 1980. Implications of regional gravity for state of stress in the earth's crust and upper mantle, *J. geophys. Res.*, 85, 6377-6396.
- Melosh, H. J., 1978. Dynamic support of the outer rise, *Geophysical Research Letters*, 5, 321-324.
- Melosh, H. J. & Raefsky A., 1980. The dynamical origin of subduction zone topography, *Geophys. J. R. astr. Soc.*, 80, 333-354.
- Murrell, S. A. F., 1976. Rheology of the lithosphere-experimental indications, *Tectonophysics*, 36, 5-24.
- Parsons, B. & Molnar, P. 1976. The origin of outer topographic rises associated with trenches, *Geophys. J. R. astr. Soc.*, 45, 707-712.
- Pearson, C. E., 1959. Theoretical Elasticity, Harvard Univ. Press, Cambridge, Mass., p. 120.
- Peltier, W. R. & Andrews, J. T., 1976. Glacial-isostatic adjustment, I, the forward problem, *Geophys. J. R. astr. Soc.*, 46, 605-646.
- Ross, D. A. & Shor, Jr., G. G., 1965. Reflection profiles across the Middle America Trench, *J. geophys. Res.*, 70, 5551-5572, 1965.
- Ruff, L. & Kanamori, H., 1980. Seismicity and the subduction process, *Physics of the Earth and Planetary Interiors*, 23, 240-252.
- Sleep, N. H., 1981. Origin of topography and gravity anomalies at subduction zones, *Tectonophysics*,
- Stevenson, D. J. & Turner, J. S., 1977. Angle of subduction, *Nature*, 270, 334-336.

- Tomoda, Y. & Fujimoto, H. 1982. Maps of gravity anomalies and bottom topography in the western Pacific and reference book for gravity and bathymetric data, *Bull. Ocean Res. Inst.*, Univ. Tokyo, No. 14.
- Tovish, A., Schubert, G. & Luyendyk, B. P., 1978. Mantle flow pressure and the angle of subduction: non-Newtonian corner flows, *J. geophys. R.*, 83, 5892-5898.
- Turcotte, D. L. & Oxburgh, E. R., 1967. Finite amplitude convective cells and continental drift, *J. Fluid Mech.*, 28, 29-42.
- Turcotte, D. L., MacAdoo, D. C. & Caldwell, J. G., 1978. An elastic-perfectly plastic analysis of the bending of the lithosphere at a trench, *Tectonophysics*, 47, 193-205.
- Turcotte, D. L., Schubert, G., 1982. *Geodynamics, Application of Continuum Physics to Geological Problems*, John Wiley and Sons, New York.
- Uyeda, S. & Kanamori, H., 1979. Back-arc opening and the model of subduction, *J. geophys. Res.*, 84, 1049-1061.
- Walcott, R. I., 1970. Flexural rigidity, thickness and viscosity of the lithosphere, *J. geophys. Res.*, 75, 3941-3954.
- Watts, A. B. & Talwani, M., 1974. Gravity anomalies seaward of deep-sea trenches and their tectonic implications, *Geophys. J. R. astr. Soc.*, 36, 57-90.
- Watts, A. B. Cochran, J. R. & Selzer, G., 1975. Gravity anomalies and flexure of the lithosphere: A three-dimensional study of the Great Meteor Seamount, Northeast Atlantic, *J. geophys. Res.*, 80, 1391-1398.
- Watts, A. B., Bodine, J. H. & Steckler, M. S., 1980. Observations of flexure and the state of stress in the oceanic lithosphere, *J. geophys. Res.*, 85, 6369-6376.
- Yoshii, T., 1979. A detailed cross-section of the deep seismic zone beneath northeastern Honshu, Japan, *Tectonophysics*, 55, 349-360.

Figure captions

Figure 1. (a) Geometry for corner flow in region A. (b) The geometry of a simple subducting slab model with dip angle θ . The slab has a constant thickness in the direction normal to the top surface, which is composed of two straight lines connecting a circular arc DC with radius b and center A. The bottom surface is concentric with the top surface and has radius a .

Figure 2. Pressure profiles measured at two different dimensionless depths d in the bending slab model. Dashed lines show p_r , the pressure which is calculated by finite element methods and which has a minimum value (tensional) at $x = 0$ (Fig 1(b)). Solid lines show p_a , the pressure which is calculated with the analytic formula (32). The scales are different for each depth, and are normalized relative to the minimum pressure.

Figure 3. (a) Pressure contours for the circular-arc grid with constant tangential velocity boundary condition on the top surface. 1470 isoparametric bilinear elements, distributed according to the numbers on the sides of the grid, were used. The velocity vectors on the beginning and end of the grid are parallel to the upper surface of the slab and have unit magnitude. The bottom surface of the slab is traction free. (b) Pressure profile at the upper surface of the slab.

Figure 4. (a) Pressure contours for a circular arc grid with smoothed velocity boundary conditions on top surface. The bottom surface boundary conditions are the same as those stated in Figure 4. (b) Pressure profile for the layer at distance $d = 0.005$ from the upper surface.

Figure 5. Three error function velocity profiles (a-1), (a-2), and (a-3).

determined from formula (35) with $v = 1.0$, $\theta = 45^\circ$, and $S_c = 0.8, 0.4$, and 0.2 respectively. (b-1), (b-2), and (b-3) are the pressure profiles along the top line of the circular-arc grid with velocity profiles (a-1), (a-2), and (a-3) applied respectively. (c-1), (c-2), and (c-3) are for the rectangular grid with the same velocity boundary conditions (a-1), (a-2), and (a-3).

Figure 6. The velocity vectors of a small segment of the stream line projected onto two characteristic directions. Near the bend axis the tangential velocity gradient is zero and the normal velocity gradient is constant.

Figure 7. Superposition of the pressure due to normal gradients. The 10 thin lines are pressure profiles calculated using the fundamental solution in Table 1 for a vertical step function velocity boundary condition. The parameters used in the formula are $\eta = 1.0$, $y = -0.005$, and $x = 0, \pm 1.0, \pm 0.75, \pm 0.50, \pm 0.25$. The thick line is a pressure profile which sums these 10 individual pressure profiles.

Figure 8. The pressure along the top line of the circular arc slab model calculated using the finite element method. (a - 1) Velocity boundary conditions as a function of horizontal distance applied to the circular arc boundary of the grid shown as Figure 3(a), where the thickness $H_v = 1$, radius $R = 1.85$, dip angle $\theta = 45^\circ$, and where ($x = 0$) corresponds to the beginning of the arc. A_x and A_y are the horizontal (seaward) and vertical (upward) velocity components, v_x and v_y in formula (33) of the text, respectively. These velocity profiles have discontinuous first derivatives at the two ends of the circular arc section. Curves B_x and B_y are smoothed versions of A_x and A_y (i.e. v_x and v_y in formula (34) of the text, which have a continuous first derivative). C_x and C_y are the differences between B_x and A_x , and B_y and A_y respectively. (a - 2) The

differential velocities C_x and C_y , plotted on a coordinate system which has the origin at the middle of the circular arc. (b - 1), (b - 2), (b - 3) are pressure profiles along the top surface of the circular arc grid, which correspond to the velocity boundary conditions A_x and A_y , C_x and C_y , and B_x and B_y respectively. (c - 1) and (d - 1) are schematic normal velocity gradients g_{\perp} for the velocity boundary condition of A_x and A_y , and g'_{\perp} for the differential velocity boundary condition C_x and C_y . The pressure profiles for the normal velocity gradients g_{\perp} and g'_{\perp} are shown in (c - 2) and (d - 2). (e) A diagram which illustrates how to obtain the normal velocity gradient g_{\perp} and tangential velocity gradient g_{\parallel} for a constant tangential velocity boundary condition on the circular arc. The tangential velocity gradient g_{\parallel} is zero, and the normal velocity gradient g_{\perp} is a constant on the the entire arc.

Figure 9. Two finite element grids used in the present calculations, which have slightly different geometries for the top line of the grid. The horizontal solid lines above each grid are the x-axis (at sea level). The trench axis off Northern Honshu, Japan is located at $x = 0$. The dotted line beneath the x-axis is the averaged topography data of Northern Honshu. Hypocenters of low-angle thrust and down-dip compressional events of Northern Honshu, Japan are plotted as dots below the topography line. Above the grids the horizontal velocities v_x (landward) and vertical velocities v_y (downward) are plotted. The top line of the grid in (a), called model A in the text, is a polynomial obtained by a least squares fit to the topography and upper envelope of the hypocenters. The top line of the grid in (b), called model B, is a polynomial which fits the topography and upper envelope of the hypocenters slightly differently.

Figure 10. The bathymetric profile east of Northern Honshu. The seaward side of the profile is obtained by averaging 5 profiles ranging from 450 km

west to 900 km east of the trench axis. These cross sections correspond to the boundaries of the 4 seismicity cross sections used by Kawakatsu and Seno (1983). The top lines of the two finite element grids, for model A and model B are also plotted.

Figure 11. The stress components T_{xx} , T_{yy} , and pressure P as functions of distance from trench for the top (a) and bottom (b) surface of the model A with a Newtonian constitutive law.

Figure 12. The contours for stress components T_{xx} (a), T_{yy} (b), and pressure P (c), and the deviatoric compressional principal stress (d) for model A with Newtonian constitutive law. The length of the small lines plotted in (d) is proportional to the magnitude of the compressional principal stress and their orientation is parallel to the direction of the compressional principal stress.

Figure 13. The stress components T_{xx} , T_{yy} , and pressure P as functions of distance from trench for the top (a) and bottom (b) surface of the model A with a non-Newtonian constitutive law (power law 3).

Table 1
Fundamental Solutions

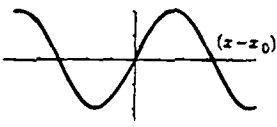
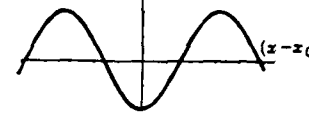
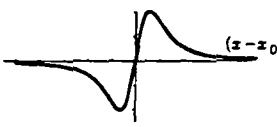
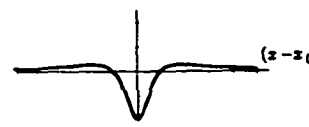
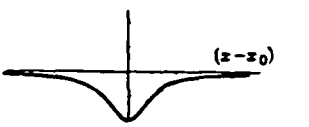
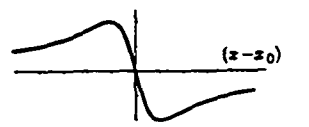
<p>- 1 -</p> <p>Boundary condition $v_x(x,0) = \cos \lambda x,$ $v_y(x,0) = 0, \quad \lambda > 0$</p> <p>Stream function $\psi(x,y)$ $y e^{\lambda y} \cos \lambda x$</p> <p>Pressure $p(x,y) - p(x,-\infty)$ $2\eta \lambda e^{\lambda y} \sin \lambda x$</p>	<p>- 2 -</p> <p>Boundary condition $v_x(x,0) = 0,$ $v_y(x,0) = \cos \lambda x, \quad \lambda > 0$</p> <p>Stream function $\psi(x,y)$ $(y - \frac{1}{\lambda}) e^{\lambda y} \sin \lambda x$</p> <p>Pressure $p(x,y) - p(x,-\infty)$ $-2\eta \lambda e^{\lambda y} \cos \lambda x$</p>	<p>- 3 -</p> <p>Boundary condition $v_x(x,0) = \delta(x-x_0),$ $v_y(x,0) = 0$</p> <p>Stream function $\psi(x,y)$ $-\frac{1}{\pi} \frac{y^2}{(x-x_0)^2 + y^2}$</p> <p>Pressure $p(x,y) - p(x,-\infty)$ $-\frac{\eta}{\pi} \frac{4(x-x_0)y}{[(x-x_0)^2 + y^2]^2}$</p>
<p>$p(x,y) - p(x,-\infty)$</p> 	<p>$p(x,y) - p(x,-\infty)$</p> 	<p>$p(x,y) - p(x,-\infty)$</p> 
<p>- 4 -</p> <p>Boundary condition $v_x(x,0) = 0,$ $v_y(x,0) = \delta(x-x_0)$</p> <p>Stream function $\psi(x,y)$ $\frac{1}{\pi} \left\{ \frac{(x-x_0)y}{(x-x_0)^2 + y^2} - \arccot \cot \frac{x-x_0}{y} \right\}$</p> <p>Pressure $p(x,y) - p(x,-\infty)$ $-\frac{2\eta}{\pi} \frac{y^2 - (x-x_0)^2}{[(x-x_0)^2 + y^2]^2}$</p>	<p>- 5 -</p> <p>Boundary condition $v_x(x,0) = H(x-x_0),$ $v_y(x,0) = 0$</p> <p>Stream function $\psi(x,y)$ $\frac{1}{\pi} y \arccot \cot \frac{x-x_0}{y}$</p> <p>Pressure $p(x,y) - p(x,-\infty)$ $\frac{\eta}{\pi} \frac{2y}{(x-x_0)^2 + y^2}$</p>	<p>- 6 -</p> <p>Boundary condition $v_x(x,0) = 0,$ $v_y(x,0) = H(x-x_0)$</p> <p>Stream function $\psi(x,y)$ $\frac{1}{\pi} \left\{ y - (x-x_0) \arccot \cot \frac{x-x_0}{y} \right\}$</p> <p>Pressure $p(x,y) - p(x,-\infty)$ $-\frac{\eta}{\pi} \frac{2(x-x_0)}{(x-x_0)^2 + y^2}$</p>
<p>$p(x,y) - p(x,-\infty)$</p> 	<p>$p(x,y) - p(x,-\infty)$</p> 	<p>$p(x,y) - p(x,-\infty)$</p> 

Table 2

	Predicted Topography			Observed topography
	Viscous plate	Elastic plate over viscous plate $E = 0.7 \times 10^{11}$ Pa		
		$H_e = 15$ km $D_c = 2.1 \times 10^{22}$ $\alpha = 44$ km	$H_e = 30$ km $D_c = 1.7 \times 10^{23}$ $\alpha = 74$ km	
x_t km	-200	-180	-170	0
w_t m	-300	-270	-220	-1500
x_r km	140	130	130	150
w_r m	20	9	11	500

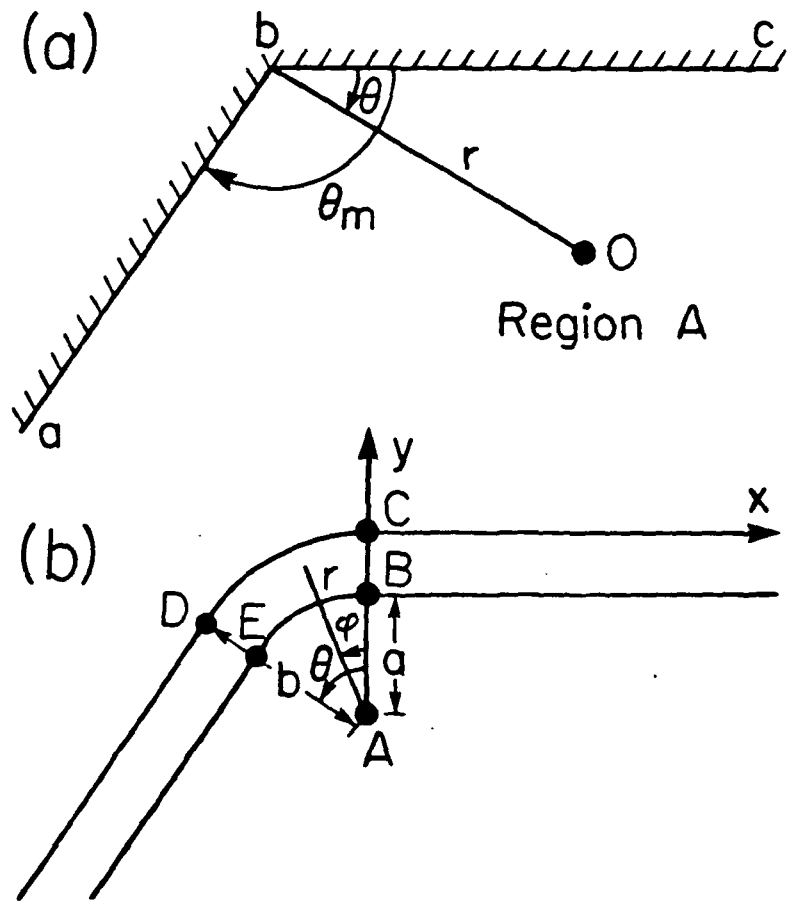


Fig. 1

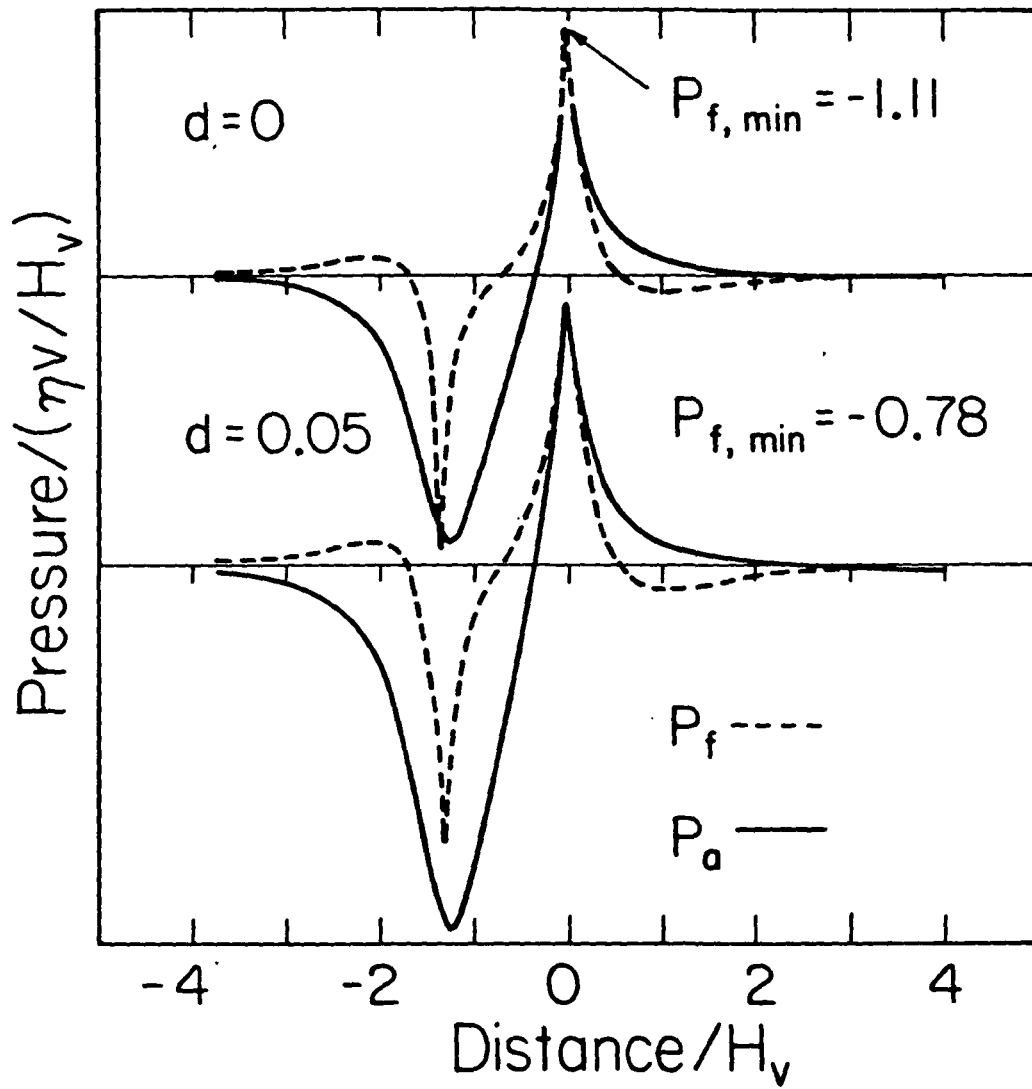


Fig. 2

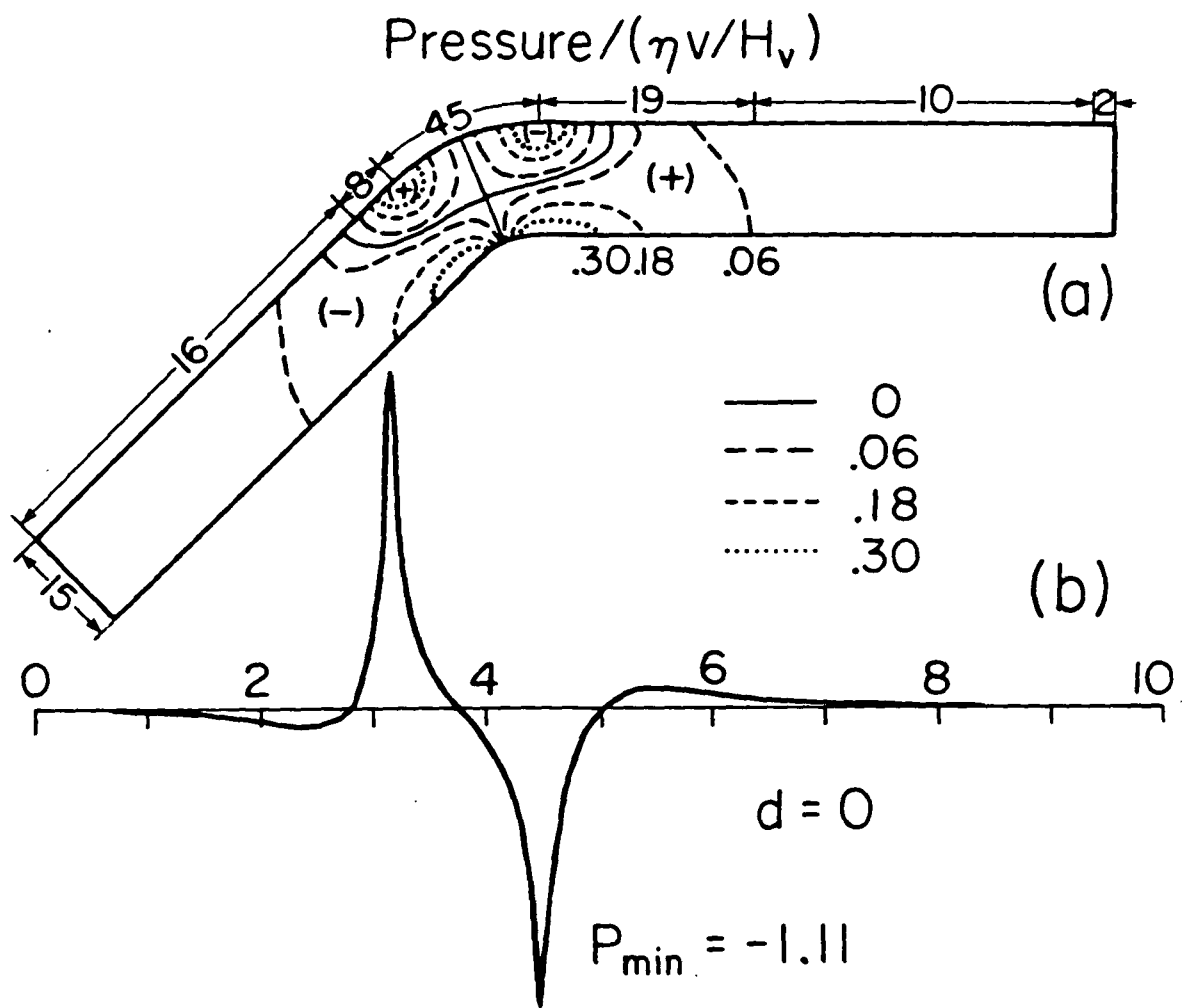


Fig. 3

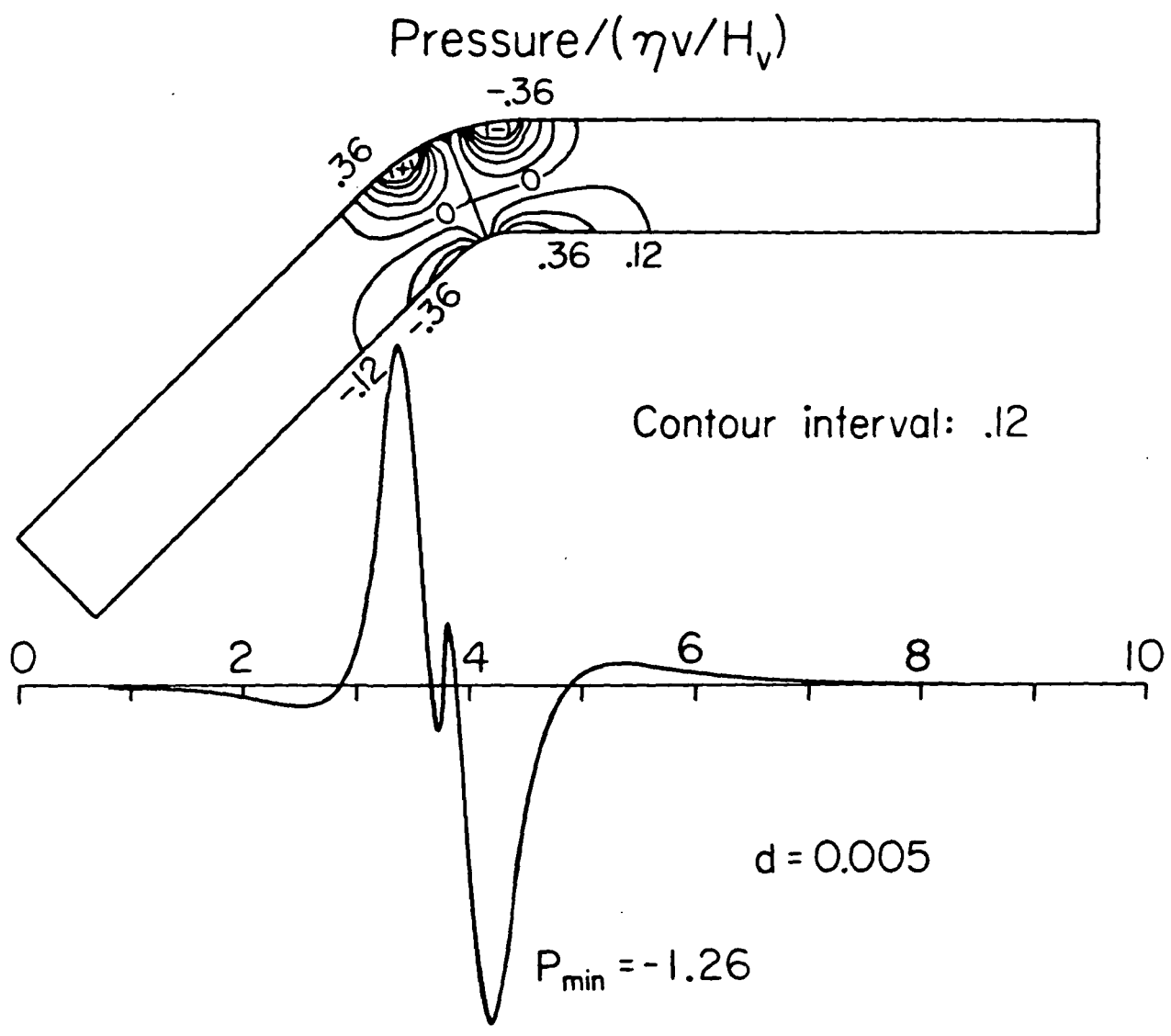


Fig. 4

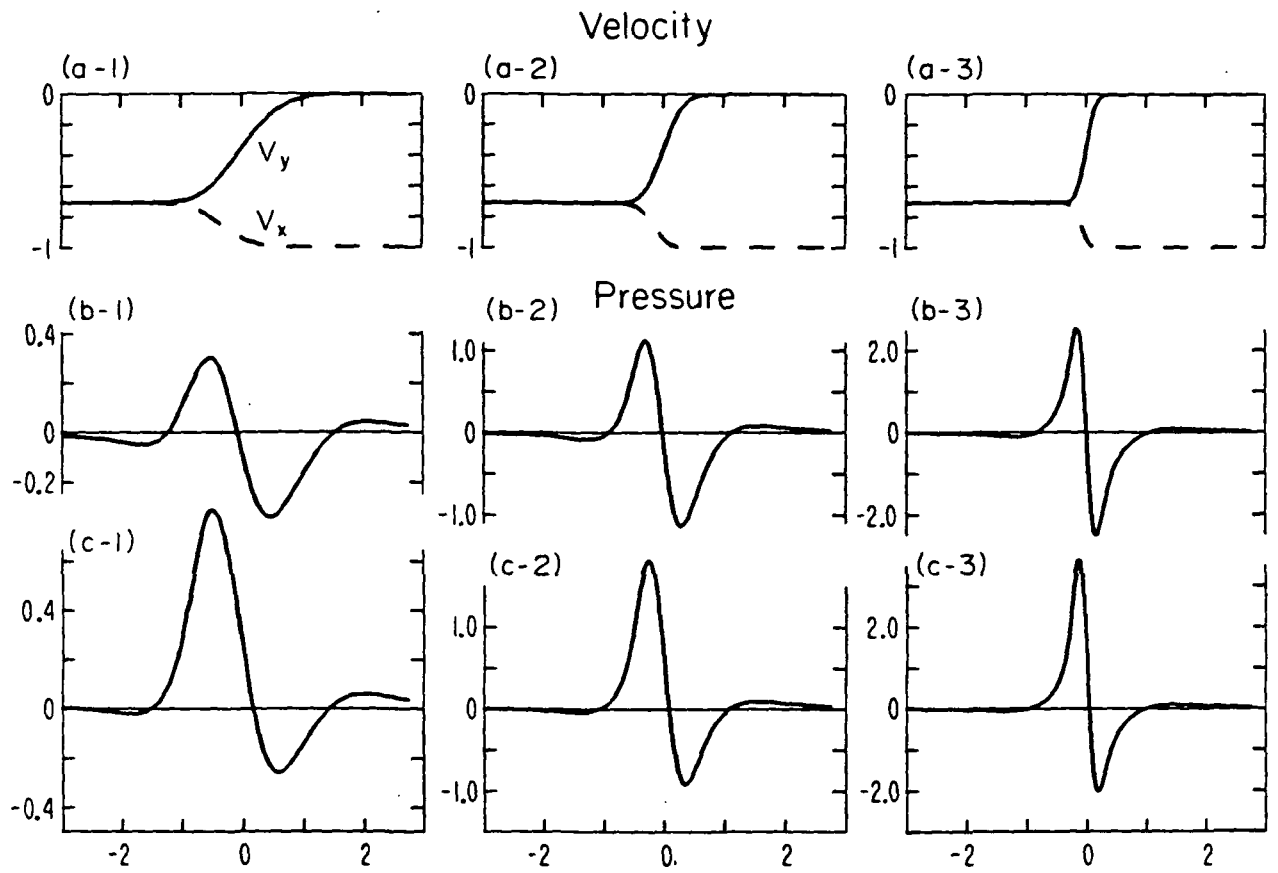


Fig. 5

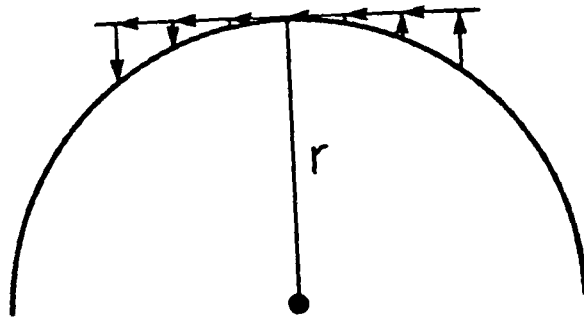


Fig. 6

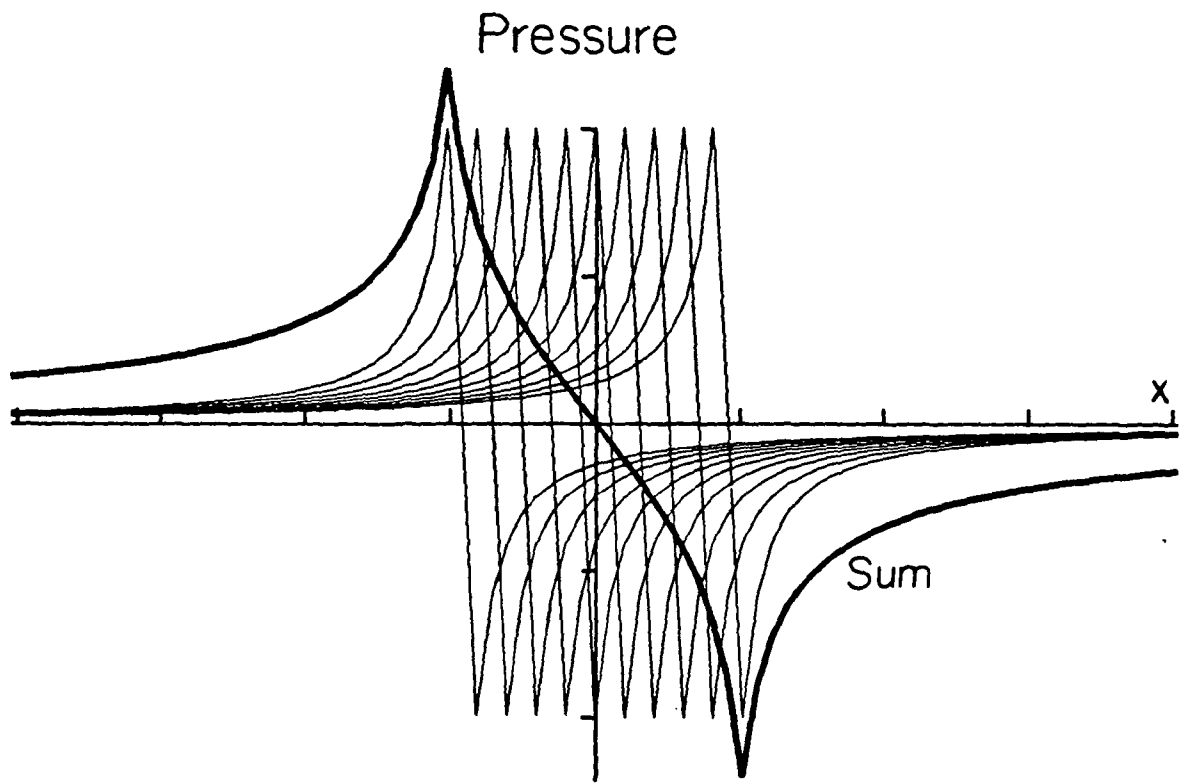


Fig. 7

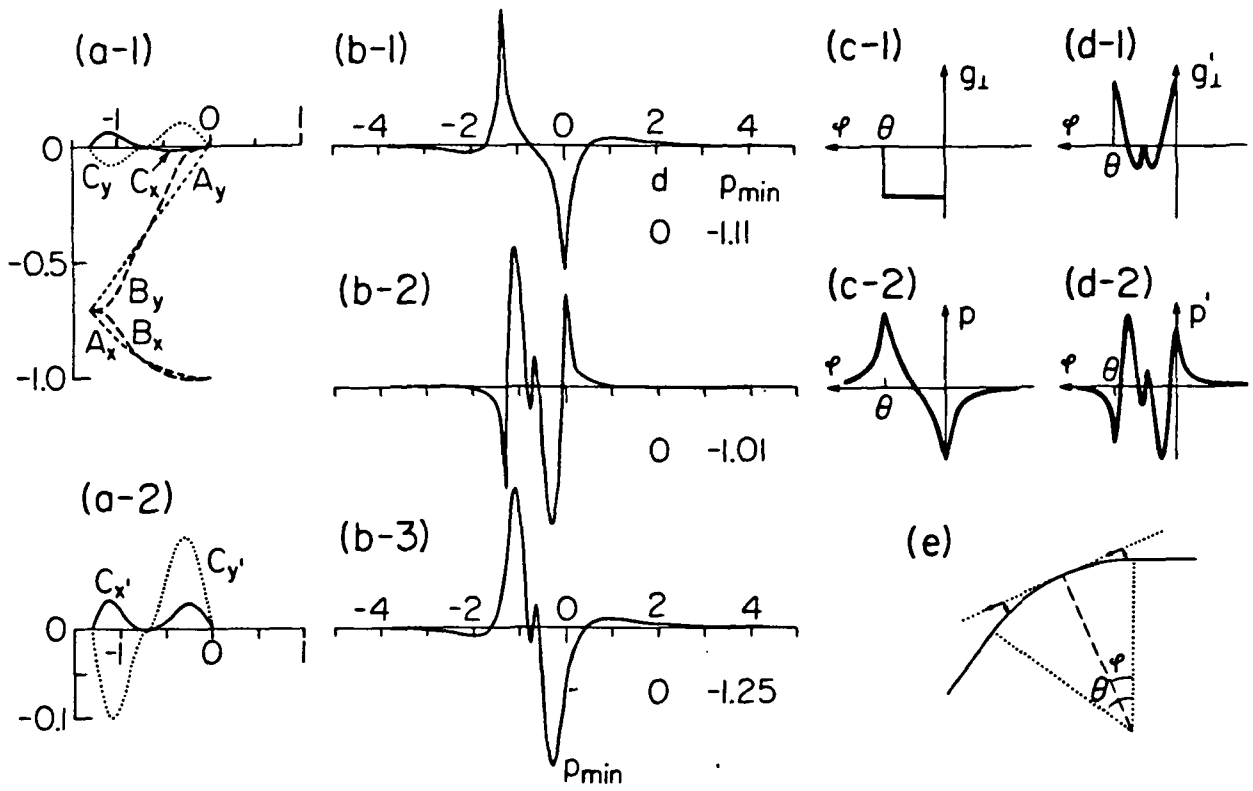


Fig. 8

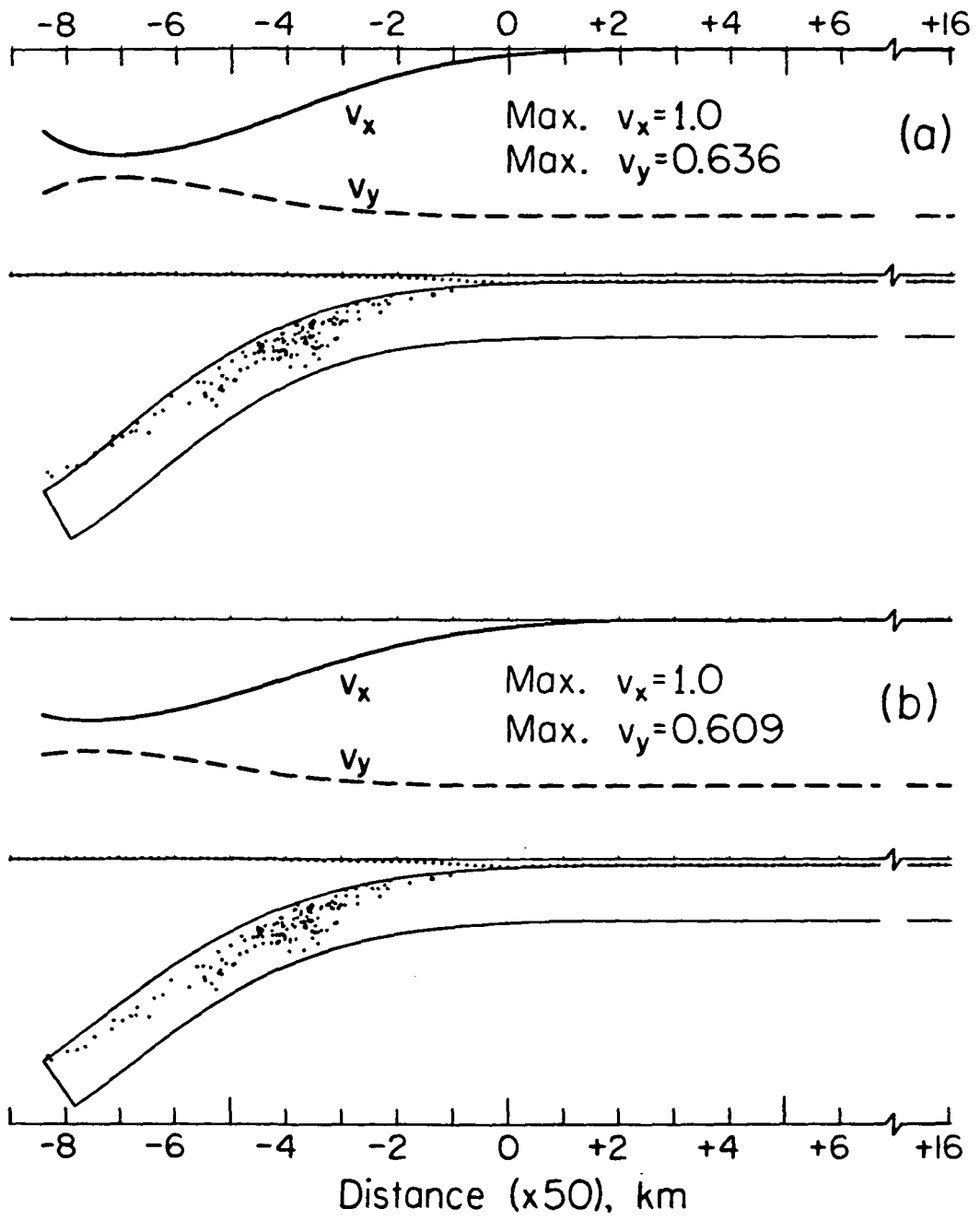


Fig. 9

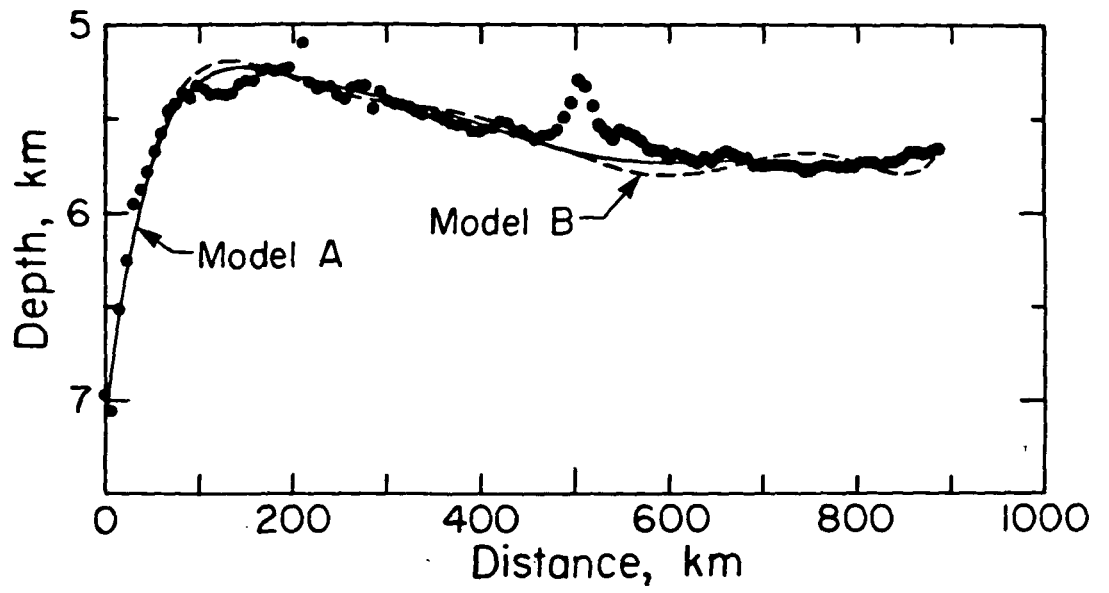


Fig. 10

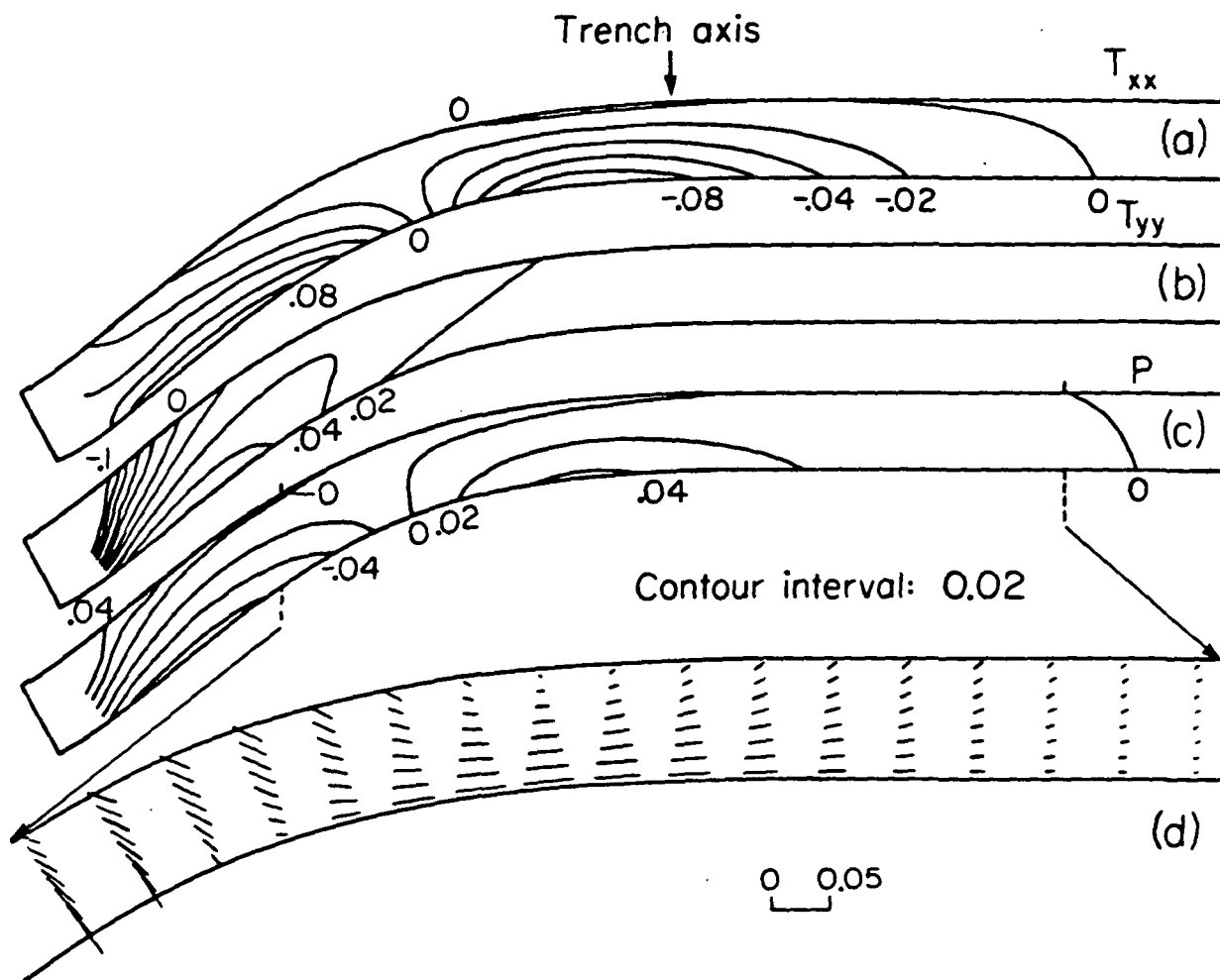


Fig. 12

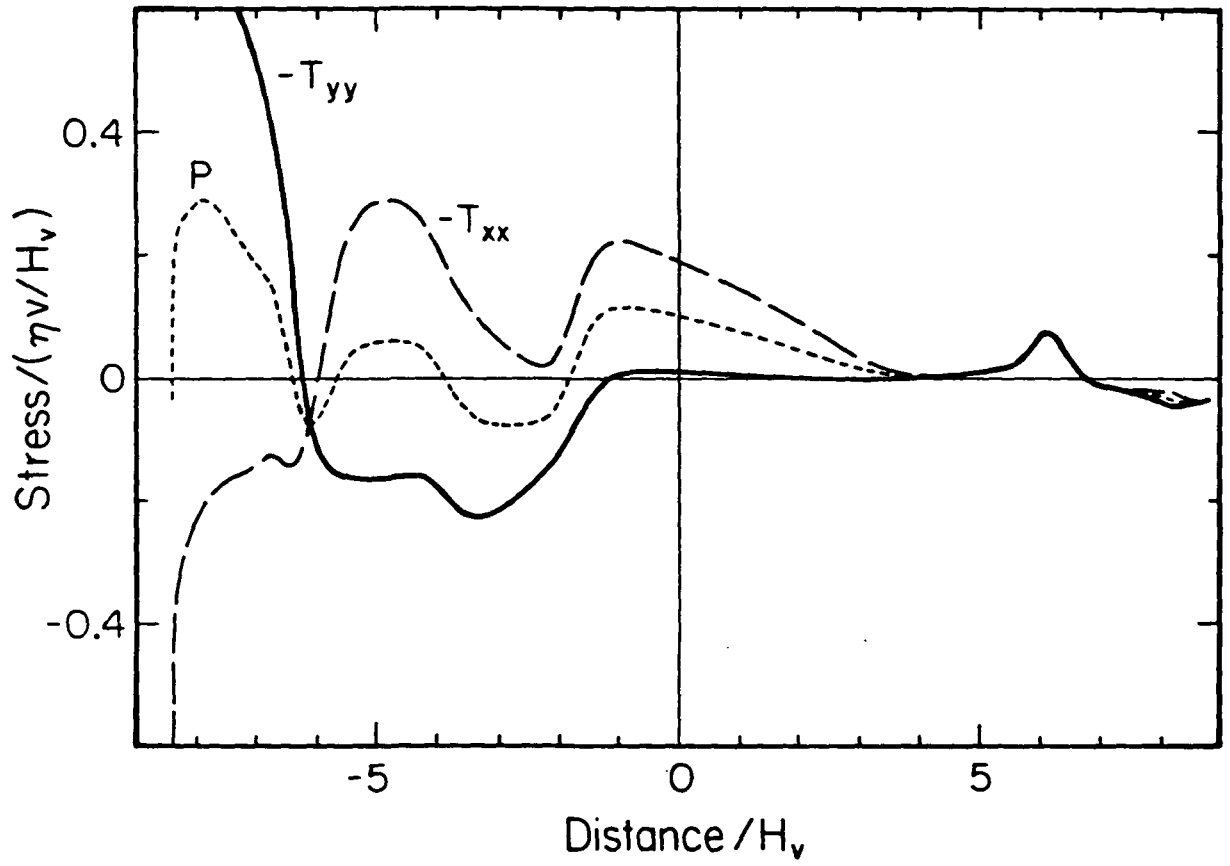


Fig. 13